Optimal Integration Schemes for Polygonal Finite Element Method with Schwarz-Christoffel Conformal Mapping

A Project Report

Submitted in partial fulfilment of the

requirements for the Degree of

Master of Engineering

in

Aerospace Engineering

by

Satyendra Singh

Department of Aerospace Engineering

Indian Institute of Science

BANGALORE – 560 012

June 2010

TO

My Teachers

Acknowledgements

I express the deepest gratitude to my supervisor, **Prof. D. Roy Mahapatra**, who has guided me throughout this project with his brilliant ideas whilst allowing me the freedom to work in my own way. His energy and enthusiasm always motivated me whenever I found myself in difficult situations. It was his Applied and Computational Mechanics course that motivated me to take up the Finite Element Analysis as topic for my ME project. Without his guidance and encouragement the thesis would not have been completed.

I would like to thank **Prof. M.S. Bhatt**, Chairman, Department of Aerospace Engineering for providing me excellent work environment. I also thank the faculty members of the Aerospace department and other departments in Indian Institute of Science from whom I had the privilege to learn many concepts and fundamentals which proved to be very valuable during this project.

I would like thank my classmates and friends and particularly Pawan and Ashish who have been a great help whenever I failed to see through the sometimes obvious and other times not so obvious things.

In addition I would like to thank, Sundararajan Natarajan, Phd scholar, Cardiff University, Wales, U.K and Stéphane Bordas, Professor, Cardiff University, Wales, U.K for constantly being in touch through emails and providing support whenever needed.

I would also like to thank my parents who have always taught me to follow my heart no matter what obstacles I might encounter. I am greatly indebted to them for their unconditional support and encouragement all through my life.

Publication from this work

1. Satyendra Singh, S. Natarajan, D. Roy Mahapatra, Stéphane P.A. Bordas, Optimal numerical integration schemes for polygonal finite elements. *International Journal for Numerical Methods in Engineering* 2010; (under review)

2. Satyendra Singh, S. Natarajan, D. Roy Mahapatra, Stéphane P.A. Bordas, Extended Polygonal Finite Elements with a Optimized Numerical Integration Scheme for Linear Elastic Fracture Problems. *International Journal for Numerical Methods in Engineering*; (to be submitted)

Contents

List of Tables

List of Figures

Abstract

This thesis presents numerical integration schemes for Polygonal Finite Elements with Schwarz-Christoffel mapping which are optimal with superconvergent properties. The arbitrary polygons of a finite element mesh are first mapped to regular polygons using isoparametric mapping and then to the unit-disk using SchwarzChristoffel mapping. Numerical integration is done over this unit-disk by determining optimized integration points. Lowest order Gauss quadrature points on isoparametrically mapped domain are considered as initial conditions for optimization. Hence this method achieves better accuracy and faster convergence compared to other contemporary methods with fewer computational resources. The method automatically reduces to standard Gauss quadrature based integration when polygons are quadrilaterals as a special case. Numerical results presented for a few benchmark problems show high accuracy of the proposed schemes. The method is established considering structured as well as unstructured meshes consisting of pentagons and hexagons which, is a significant step forward to meshing complicated geometry and interfaces, material microstructure etc. Application of numerical integration using optimal integration points for linear elastic fracture mechanics problem in polygonal extended finite elements framework is considered next . Optimal integration scheme is used for numerical integration over polygonal finite elements. Stress intensity factors are computed for pure mode 1 and mixed mode cases using structured quadrilateral and structured hexagonal meshes. The results are compared to standard isoparametric extended finite element method with quadrilateral elements. The method is shown to have good accuracy and convergence with respect to the existing methods

Keywords

Polygonal Finite Element, Shawarz-Christoffel conformal Mapping, Extended Finite Element Method, Wachspress shape function, Numerical integration, Crack, J-integral, Stress intensity factor.

Chapter 1

Introduction

1.1 Polygonal Finite Element Method

Partial differential equations are used to formulate problems involving functions of several variables; such as fracture, propagation of sound or heat, electromagnetics, fluid flow, and elasticity. The finite element method is a powerful numerical method to solve partial differential equations. It is well established for triangular and quadrilateral elements. In case of conventional finite element method, a fine mesh is required to get an accurate result while using just the triangular elements. On the other hand sometimes it becomes very difficult to discretize complex shaped domain just by using quadrilateral mesh. These difficulties are overcome by allowing the element to have any number of edges and by performing suitably higher order interpolations. And since most of the engineering material have a polycrystalline microstructure, polygonal elements provide great opportunity to model the multi-scale physical nature of the above problem. Wachspress [11] proposed the construction of basis function on convex polygons for any number of edges. After that significant advances have been made towards construction of barycentric coordinates over arbitrary polygons [12, 13]. A simplified expression for Wachspress basis functions is presented by Meyer *et al.* [14]. Floater [15] derived barycentric coordinates in which a vertex in a planar triangulation is expressed as a convex combination of its neighboring vertices. In Refs. [13] and [16], natural neighbor interpolation is used

to construct C^0 shape functions on polygonal elements. The construction of polygonal interpolants using the principle of maximum entropy is described in Ref. [17]. Despite all the advantages, use of polygonal elements poses one difficulty similar to meshfree methods [18] and XFEM. Since the approximation functions for polygons are usually non-polynomial, numerical integration becomes a problem. Several schemes have been proposed to integrate this kind of approximation over polygonal domains to obtain the stiffness matrix. One such scheme is to map a polygon in physical space to a regular polygon [13, 16]. This regular polygon is then divided into triangles. These triangles are then mapped to reference triangle and numerical quadrature rules over triangle are used for numerical integration [19]. Hence two levels of mapping are required in this scheme. Natarajan *et al.* [20] proposed mapping of an arbitrary polygon to a unit-disk using Schwarz-Christoffel conformal mapping and used a mid-point integration [21] rule to integrate stiffness terms over a polygonal element. This method eliminates the need for two-level mapping involving isoparametric polygonal mapping and triangulation. However, the method still suffers from two existing disadvantages. First of all it is expensive to compute the Schwarz-Christoffel map for each polygon. And secondly a large number of integration points, around 20 or more, are required to get accurate results of numerical integration while using the mid-point integration rule. According to the mid-point integration rule, the integration points are placed at the centroid of each polar segments of the polygon. However, a significant improvement on element performance was proved in Ref. [20] and more needs to be done.

1.2 Extended Finite Element Method

Finite element method has been used in fracture mechanics applications. Chan *et al.* [1] have shown the usefulness of finite element method in computation of crack tip stress intensity factors. Li *et al.* [2] compared two different methods for the calculation of energy release rates. However in all the conventional finite element methods, the mesh should conform to crack geometry. This imposes a major constraint on meshing and

remeshing in case of crack growth problems. Babuska *et al.* [43] proposed a new type of finite element method called Partition of Unity Method (PUM). The method introduced the ability to include in the finite element space knowledge about the partial differential equation being solved by including the local enrichment functions in the finite element approximation. Later on this concept of the PUM is utilized to represent the arbitrarily oriented crack within the finite element mesh by means of enrichment functions [3, 4]. This method later came to be known as eXtended Finite Element Method (XFEM) [5]. The XFEM has been implemented in the polygonal framework [44]. In Polygonal XFEM, similar to XFEM on quadrilateral meshes, due to the presence the discontinuous enrichment functions and high strain gradient regions near crack tips special care has to be taken while numerically integrating the weak form of governing equation. The standard Gauss quadrature cannot be applied in elements enriched by discontinuous terms, because the Gauss quadrature implicitly assumes a polynomial approximation. This problem is overcome by partitioning the elements into subcells aligned to the discontinuity surface, in which the integrands are continuous and differentiable. Natarajan *et al.* [6] presented a method where strong and weak discontinuities could be integrated without dividing the elements into large number of sub-cells. Smoothed Finite Element Method (SFEM) combined with XFEM has also been used as one of the solutions to this problem [7]. The SFEM relies on strain smoothing, which was proposed by Chen *et al.* [8] for meshless methods. Natarajan *et al.* [9] proposed a new method by coupling the SFEM with the XFEM, a new numerical method called the Smoothed eXtended Finite Element Method (SmXFEM).

As mentioned previously Tabarraei *et el.* [44] applied the XFEM method in polygonal framework. In order to obtain the numerical integration of the weak form for governing differential equation they subdivided the enriched elements into triangles. Then they used well known quadrature rules for triangle for numerical integration. Since no well established method exists for integrating over polygonal elements they used the triangulation scheme for unenriched elements too. This however requires huge computational resources.

1.3 Scope of this Thesis

In this thesis a new approach has been proposed. A two-level mapping is used as described next. First the arbitrary polygons in physical space are mapped to a regular reference polygon using isoparametric mapping. Wachspress shape functions are defined over these regular polygons. These regular polygons are then mapped to a unit-disk using Schwarz-Christoffel conformal mapping. Then optimized integration points according to the procedure outlined in section 3.2 are obtained for numerical integration. The Schwarz-Christoffel map is computed only once for the reference polygon irrespective of the arbitrary shape of the polygons in physical space, which is very similar to one time computation of integrals in the isoparametric family of polynomial finite element meshes. Only the Jacobian of the isoparametric mapping needs to be computed for all polygonal elements.

The optimal integration scheme is then used for linear elastic fracture mechanics problems in XFEM framework. The optimal numerical integration technique is used for arbitrary polygonal domains to compute the stiffness matrix for unenriched polygonal elements. The triangulation scheme is used in case of enriched elements. This results in large saving of computational resources as only the enriched elements, which are small fraction of overall mesh, needs to be triangulated.

The outline of this thesis is as follows. In chapter 2 formulation of polygonal finite element method is presented. The basic equations of linear elasticity are revisited in section 2.1. We will briefly recall the formulation and the construction of polygonal finite elements in section 2.2 and discuss the construction of Wachspress shape functions in section 2.3. We discuss the numerical integration of weak form of governing equation in section 2.4 and give brief introduction to Schwarz-Christoffel mapping in section 2.5 and proposed integration scheme is discussed next. In chapter 3 we discuss the two-level mapping and propose two different optimization schemes of numerical integration. Few benchmark problems for comparison of results are considered next. SC mid-point method using 6 integration points is used to compare the performance of the proposed two optimal integration schemes. Results are compared for structured as well as unstructured

meshes with quadrilaterals, pentagons and hexagons. It is to be noted that the polygonal elements we are referring to in this thesis have no mid-side nodes. That is, there are 4,5 and 6 nodes in quadrilateral, pentagonal and hexagonal elements, respectively.

In Chapter 4 we give the formulation of XFEM for crack problems. Section 4.1 briefly revisits basic equations of linear elasticity for crack problems. Section 4.2 discusses the crack modeling using discontinuous enrichment. Issues related to integration of discontinuous functions and implementation of optimal integration scheme for extended finite element method is considered in section 4.3. Numerical examples are presented in Section 4.4. This is followed by conclusions in chapter 5.

Chapter 2

Problem Formulation

2.1 Governing Equations and Weak Form

The governing equilibrium equations for a two-dimensional linear static elasticity problem defined in the domain Ω bounded by Γ and $\Gamma = \Gamma_u \cup \Gamma_t$, $\Gamma_u \cap \Gamma_t = \phi$ is given by

$$\nabla_s^{\mathrm{T}} \boldsymbol{\sigma} + \mathbf{b} = \mathbf{0} \quad \text{in } \Omega \tag{2.1}$$

where $\mathbf{0}$ is a null vector, $\boldsymbol{\sigma}$ is the stress tensor and $\mathbf{b}$ is the vector of external forces. The boundary conditions can be expressed as

$$\mathbf{u} = \overline{\mathbf{u}} \text{ on } \Gamma_u \tag{2.2}$$

$$\mathbf{n}^T \boldsymbol{\sigma} = \overline{\mathbf{t}} \text{ on } \Gamma_t \tag{2.3}$$

where $\overline{\mathbf{u}} = (\overline{u}_x, \overline{u}_y)^T$ is the prescribed displacement vector on the essential boundary Γ_u;

$\mathbf{t} = (\bar{t}_x, \bar{t}_y)^T$ is the prescribed traction vector on the natural boundary Γ_t; $\mathbf{n}$ is the unit outward normal vector. The discrete equations for this problem are generated using the Galerkin weak form

$$\int_{\Omega} (\bigtriangledown_s \delta\mathbf{u})^T \mathbb{D} (\bigtriangledown_s \mathbf{u}) d\Omega - \int_{\Gamma} (\delta\mathbf{u}^T)\mathbf{b} d\Omega - \int_{\Gamma} (\delta\mathbf{u})^T \bar{\mathbf{t}} d\Gamma = 0 \tag{2.4}$$

where $\mathbf{u}$ and $\delta\mathbf{u}$ are the test functions that belong to admissible functions from Sobolev space and $\mathbb{D}$ is the constitutive matrix. The finite element method uses the following trial functions $\mathbf{u}^h(\mathbf{x})$ and the test functions $\delta\mathbf{u}^h(\mathbf{x})$:

$$\mathbf{u}^h(\mathbf{x}) = \sum_{i=1}^{N_P} \mathbf{N}_i(\mathbf{X})\mathbf{u}_i, \quad \delta\mathbf{u}^h(\mathbf{x}) = \sum_{i=1}^{N_P} \mathbf{N}_i(\mathbf{X})\delta\mathbf{u}_i \tag{2.5}$$

where N_P is the total number of nodes in the mesh.

$$\mathbf{N}_i = \begin{bmatrix} N_i & 0 \\ 0 & N_i \end{bmatrix} \tag{2.6}$$

is the shape functions matrix with entries being a polynomial of degree p or a rational polynomial associated with node i, $\mathbf{u}_i = [u_i, v_i]^T$ are the degrees of freedom associated with node i. By substituting the approximations $\mathbf{u}^h$ and $\delta\mathbf{u}^h$ into the weak form and invoking the arbitrariness of virtual nodal displacements, Equation (2.4) yields the standard discretized algebraic system of equations:

$$\mathbf{K}\mathbf{u} = \mathbf{f} \tag{2.7}$$

with the stiffness matrix given by

$$\mathbf{K} = \int_{\Omega^h} \mathbf{B}^\mathbf{T}\mathbf{D}\mathbf{B} d\Omega \tag{2.8}$$

and the load vector given by

$$\mathbf{f} = \int_{\Omega^h} \mathbf{N}^\mathbf{T}\mathbf{b} d\Omega + \int_{\Gamma_t} \mathbf{N}^\mathbf{T}\bar{\mathbf{t}} d\Gamma \tag{2.9}$$

where Ω_h is the discretized domain, formed by the union of elements Ω_e. The stiffness matrix $\mathbf{K}$ is symmetric, positive definite and with a strain-displacement matrix defined

as

$$\mathbf{B}_i(\mathbf{x}) = \bigtriangledown_s N_i(\mathbf{x}) = \begin{bmatrix} \frac{\partial N_i}{\partial x} & 0 \\ 0 & \frac{\partial N_i}{\partial y} \\ \frac{\partial N_i}{\partial y} & \frac{\partial N_i}{\partial x} \end{bmatrix} \tag{2.10}$$

where i in equation (2.10) corresponds to node i of the element. The size of the $\mathbf{B}$ matrix depends on the number of nodes in a polygonal element. In this thesis we consider the nodes only at the vertices of the polygonal elements.

2.2 Approximations on Polygons

Consider a polygonal domain $\Omega \subset \mathbb{R}^2$ that is described by n nodes. Let the i^{th} node be denoted as p_i and the coordinate of the node i is $\mathbf{x}_i = (x_i, y_i)$. Any generic point p with coordinate $\mathbf{x} = (x, y) \in \Omega$, has a set of associated shape functions $\phi_i(\mathbf{x})$. An approximation scheme for a scalar valued function $u : \Omega \to \mathbb{R}$ can be written as

$$u^h(\mathbf{x}) = \sum_{i=1}^{n} \phi_i(\mathbf{x}) u_i \tag{2.11}$$

where u_i are the unknown nodal variables at n vertices (nodes) of the polygon. From the viewpoint of a conforming Galerkin approximation, the following are some of the desirable properties of shape functions and of the resulting approximation:

1. Form a partition of unity to assure constant consistency condition, and that $\phi_i(\mathbf{x})$ is non-negative and bounded:

$$\sum_{i=1}^{n} \phi_i(\mathbf{x}) = 1, \quad 0 \leq \phi_i(\mathbf{x}) \leq 1 \tag{2.12}$$

2. Interpolate nodal data:

$$\phi_i(\mathbf{x}_j) = \delta_{ij} \tag{2.13}$$

where δ_{ij} is the Kronecker-delta. It ensures that the interpolated field at a node is identical to the nodal quantity: $u^h(\mathbf{x}_i) = u_i$.

3. Linear precision or linear completeness:

$$\sum_{i=1}^{n} \phi_i(\mathbf{x})\mathbf{x}_i = \mathbf{x} \tag{2.14}$$

   From this property it can be concluded that the shape function can exactly reproduce a linear function.

4. On the boundary of the domain Ω, the interpolant must be precisely linear, i.e. interior shape functions should not contribute if a point p lying on the convex hull and in addition only the nodes adjacent to point p must have non-zero values so that a linear interpolant is realized:

$$u^h(t) = \alpha u_1 + (1-\alpha)u_2, \;\; \mathbf{x} = \alpha\mathbf{x}_1 + (1-\alpha)\mathbf{x}_2, \;\; \mathbf{x} \in \partial\Omega, \;\; \alpha \in [0,1]. \tag{2.15}$$

Equation (2.15) in conjunction with the Kronecker-delta property in equation (2.13) ensures that essential boundary conditions can be imposed. The following methods can be used to build shape functions on polygonal domain.

1. Shape functions using length and area measures [11, 13, 16, 22] (e.g. Wachspress shape function, Metric coordinate, Rational Polynomial)
2. Natural neighbor shape functions [23, 24]
3. Maximum entropy approximant [17, 25, 26, 27, 28]
4. Barycentric coordinates on irregular *n-gon* [14, 29]

In this thesis Wachspress shape functions are used to construct interpolation function.

2.3 Wachspress Shape Functions

Using the principles of projective geometry, Wachspress constructed rational basis functions on polygonal domain [11]. In general, for an n-sided convex polygon, a Wachspress

shape function $N_i^{(n)}(x, y)$ is a polynomial of the following form:

$$N_i^n(x, y) = \frac{\mathcal{P}^{n-2}(x, y)}{\mathcal{P}^{n-3}(x, y)} \tag{2.16}$$

where $\mathcal{P}^{(m)}(x, y)$ is an m-degree polynomial in (x, y). In Ref. [14], a simple expression have been obtained for Wachspress's basis functions which can be expressed as

$$\phi_i^w(\mathbf{x}) = \frac{w_i(\mathbf{x})}{\sum_{j=1}^n w_j(\mathbf{x})} \tag{2.17a}$$

$$w_i(\mathbf{x}) = \frac{A(p_{i-1}, p_i, p_{i+1})}{A(p_{i-1}, p_i, p)A(p_i, p_{i+1}, p)} = \frac{\cot\gamma_i + \cot\delta_i}{||\mathbf{x} - \mathbf{x}_i||^2} \tag{2.17b}$$

where the last expression is due to Meyer *et al.* [14]. In equation (2.17), $A(a, b, c)$ is the

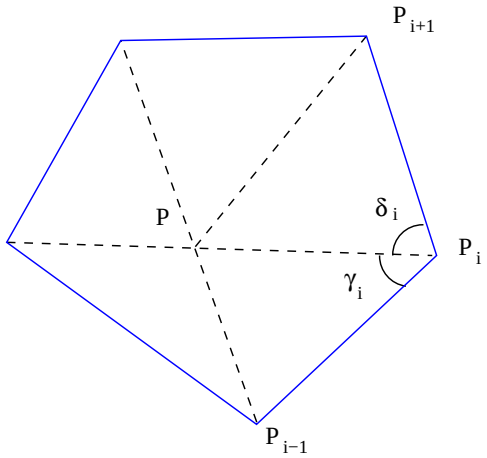

Figure 2.1: Barycentric coordinates: Wachspress basis function.

signed area of triangle $[a, b, c]$ and γ_i and δ_i are shown in figure 2.1. The signed area of a triangle whose vertices A_i have coordinates (x_i, y_i), for $1 < i < 3$, is given by [30]

$$A = \frac{1}{2}\begin{vmatrix} x_1 & y_1 & 1 \\ x_2 & y_2 & 1 \\ x_3 & y_3 & 1 \end{vmatrix} = \frac{1}{2}\left[x_3\left(y_1 - y_2\right) - y_3\left(x_1 - x_2\right) + x_1y_2 - y_1x_2\right] \tag{2.18}$$

In this thesis Wachspress shape functions are constructed by substituting the signed area of the triangle given by equation (2.18) in equation (2.17b). The Wachspress shape

functions are the functions of minimal degree that satisfy boundedness, linearity and linear dependence on convex polyshapes [31].

2.4 Numerical Integration of Weak Form

The element stiffness matrix in equation (2.8) must be evaluated over the element. In the standard polynomial finite element method, an element does not have more than four edges for 2D domains. Therefore, the Gauss quadrature rule for polynomials, which is optimal, can effectively be used to integrate the weak forms. To integrate weak forms over the *n-gon*, no general quadrature rules are available which are proved to be optimal for the integrals present in the stiffness matrices . The following methods can be used for the integration of the weak form over the *n-gon* element.

1. Sukumar and Tabarraei [13] have proposed a method to integrate the weak form over a *n-gon* element. In this method a physical element is mapped to a canonical domain and then that canonical element is subdivided into triangles and well known rules are applied on each triangle for numerical integration. This method involves a two-level isoparametric mapping: Physical element (Ω_e) $\rightarrow$ Reference polygon (Ω_o) $\rightarrow$ Triangle. The standard triangular quadrature rule is used for integration over the triangle. Moreover, in isoparametric mapping, length measures are preserved, but not the included angles, and so the positivity of the Jacobian needs to be ensured. To ensure the positivity of the Jacobian the element should be a convex element.

2. Another method to integrate over the *n-gon* element is the Smoothed Finite Element Method (SFEM) [32] which is based on strain smoothening introduced by Chen *et al.* [33] for mesh-free methods. The extension of strain smoothening to finite element method leads to integration on boundary of the finite elements, which avoids the requirement of isoparametric mapping. Even in case of the SFEM, the *n-gon* element is subdivided into triangles, solely for the purpose of numerical integration. Unlike in the triangulation scheme, in SFEM the integration points

lie on the boundary of the triangles. It was shown in Ref. [34] that Wachspress interpolant can be used to construct SFEM approximations in physical space.

3. The other method to integrate over the *n-gon* element is the method developed by Natarajan *et al.* [20]. In this method an *n-gon* element is mapped to a unit-disk using Schwarz-Christoffel conformal mapping and various cubature rules are applied for integration.

4. Recently Mousavi *et al.* [35] proposed a numerical algorithm based on group theory and numerical optimization to compute efficient quadrature rules for integration of bivariate polynomials over arbitrary polygons. They have shown that for the integration involving rational polynomial shape functions over a regular hexagon their quadrature rule requires as high as 85 integration points for a relative error of 10^{-8}.

In this thesis new method is proposed by considering the optimality of the integration points with respect to the resulting integral in the stiffness matrix. This method is described in section 2.6. In this proposed method Schwarz-Christoffel mapping is done using SCPACK [36] subroutines in FORTRAN and MATLAB SC Toolbox [37] in MATLAB.

2.5 Schwarz-Christoffel Conformal Mapping (SCCM)

Let P be the interior of a polygon Γ having vertices $w_1, ..., w_n$ and interior angles $\alpha_1\pi, ..., \alpha_n\pi$ in the counter-clockwise order. Let f be any conformal map from the unit-disk to P. Then, the Schwarz-Christoffel formula for a disk is given by [38]

$$f(z) = A + C \int^{z} \prod_{k=1}^{n} \left(1 - \frac{\zeta}{z_k}\right)^{\alpha_k - 1} d\zeta \tag{2.19}$$

for some complex constants A and C, where $w_k = f(z)\ for\ k = 1, ..., n$. The SCCM integral in equation (2.19), in general, have no exact solution and has to be solved numerically. All the necessary numerical steps are implemented using SCPACK FORTRAN library [36] and SCT Toolbox in MATLAB [37]. The Jacobian of the SCCM mapping is easily computed since the map is in an integral form and is given by

$$\frac{df}{dz} = \prod_{k=1}^{n} \left(1 - \frac{\zeta}{z_k}\right)^{\alpha_k - 1} \tag{2.20}$$

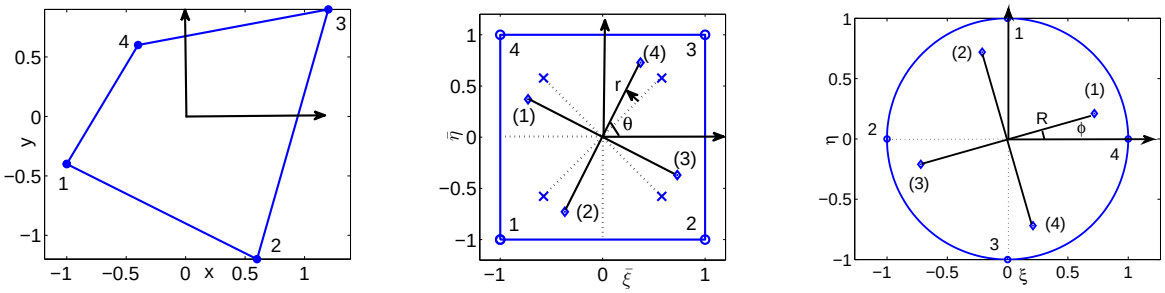

(a) (b) (c)

Figure 2.2: Two level mapping and placement of integration points for quadrilateral. Integration points are numbered and shown within parentheses. (a) Physical element. (b) Reference polygon. (c) Element mapped to unit-circle. Points connected by dotted lines in (b) are the original gauss points in standard isoparametric mapping.

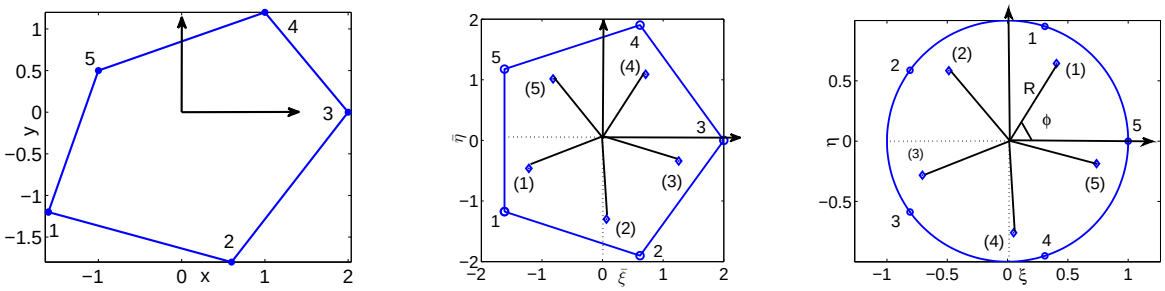

(a) (b) (c)

Figure 2.3: Two level mapping and placement of integration points for pentagon. Integration points are numbered and shown within parentheses. (a) Physical element. (b) Reference polygon. (c) Element mapped to unit-circle.

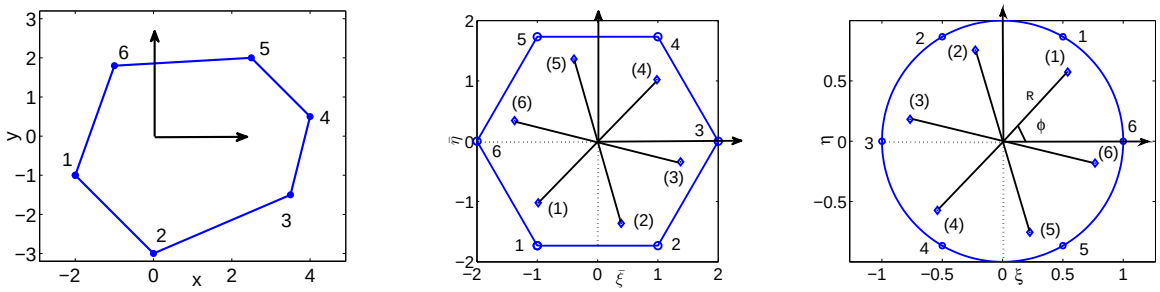

(a) (b) (c)

Figure 2.4: Two level mapping and placement of integration points for hexagon. Integration points are numbered and shown within parentheses. (a) Physical element. (b) Reference polygon. (c) element mapped to unit-circle.

2.6 Numerical Integration

In this section we describe the proposed method of numerical integration. In this scheme an arbitrary polygon in the physical domain is first mapped to a non-dimensional reference polygon using isoparametric mapping. The non-dimensional reference polygon is a regular polygon with length of its edges 2 as depicted in figures 2.2b, 2.3b and 2.4b. Details regarding mapping from physical domain to non-dimensional domain (reference polygon) can be found in ref. [13]. The reference polygon is then mapped to a unit-disk using Schwarz-Christoffel (SC) conformal mapping. Further details regarding mapping from the polygon to the unit-disk can be found in ref. [20]. Figures 2.2, 2.3 and 2.4 show the two-level mapping for quadrilateral, pentagon and hexagon respectively. Integration points are defined over unit-disk. For the present case of two-level mapping the following approximation can be used to integrate $f(x, y)$ on an element in physical space:

$$\begin{aligned}\int_{\Omega} f(x,y)dxdy &= \int_{\Omega_p} f(\bar{\xi},\bar{\eta})J_{ip}d\bar{\xi}d\bar{\eta} \\ &= \int_{\Omega_c} f(\xi,\eta)J_{ip}J_{sc}d\xi d\eta \\ &\simeq \sum_{i=1}^{n_\theta}\sum_{j=1}^{n_r} A_{ij} f(r_j\cos\theta_i, r_j\sin\theta_i)\end{aligned} \tag{2.21}$$

where θ and r are the coordinates of integration points. A_{ij}'s are the weights associated with each integration point. Weight associated is the area of segment corresponding to that integration point. J_{ip} and J_{sc} are the Jacobians associated with isoparametric and SC mapping respectively. The schemes employed to find the optimum integration points for *n-gons* are discussed in the later sections of this thesis.

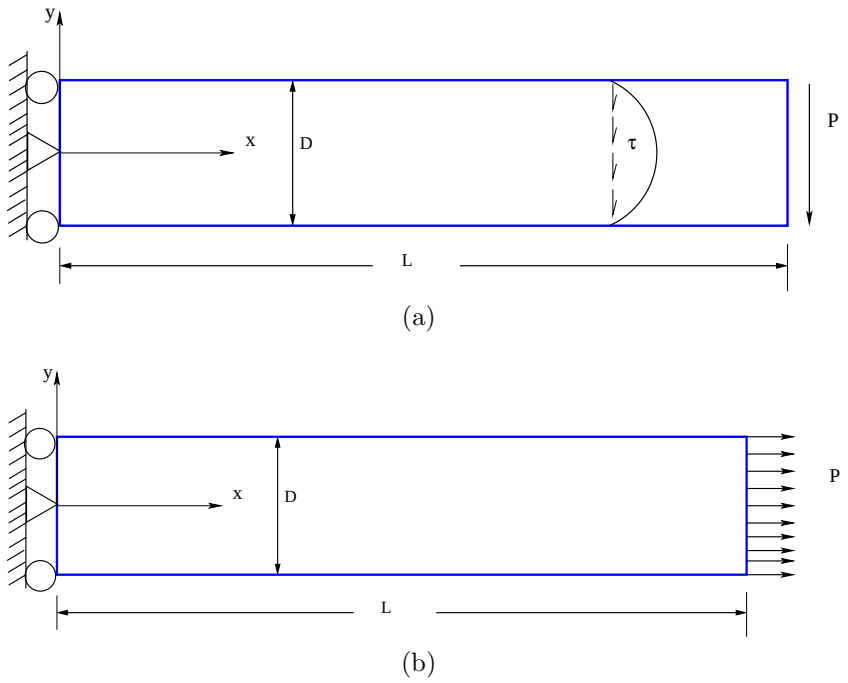

Figure 2.5: Finite element model with boundary conditions. (a) Pure shear. (b) Pure tension.

2.7 Validation Methodology

A two-dimensional cantilever beam subjected to shear and tensile loads at the free end is examined (Figure 2.5). The following geometry and material properties are used: length $L = 10$, height $D = 2$, thickness $t = 1$, Young's modulus $E = 70GPa$, Poisson's ratio $= 0.3$. A force of $100N$ is applied for shear and tensile loading cases.

The exact solution [39] for displacements and stresses for shear loading is given by

$$u(x,y) = \frac{Py}{6\overline{E}I}\left[(6L-3x)x + (2+\overline{\nu})\left(y^2 - \frac{D^2}{4}\right)\right] \tag{2.22a}$$

$$v(x,y) = -\frac{Py}{6\overline{E}I}\left[3\overline{\nu}y^2(L-x) + (4+5\overline{\nu})\frac{D^2x}{4} + (3L-x)x^2\right] \tag{2.22b}$$

where I is the second moment of inertia. Young's modulus and Poisson's ratio are, respectively

$$\overline{E} = \begin{cases} E \text{ (plane stress)} \\ \frac{E}{1-\nu^2} \text{ (plane strain)} \end{cases} \qquad \overline{v} = \begin{cases} \nu \text{ (plane stress)} \\ \frac{\nu}{1-\nu} \text{ (plane strain)} \end{cases} \tag{2.23}$$

Augarde *et al.* [40] discussed on the boundary conditions required for this exact solution given by equation (2.22). This solution holds only if the shearing forces on the ends are distributed according to the same parabolic law as the shear stress τ_{xy} and the intensity of the normal forces at the built-in end is proportional to y. Therefore the shear force at the end is applied according to the same parabolic law given by τ_{xy} as

$$\tau_{xy}(x,y) = -\frac{P}{2I}\left(\frac{D^2}{4} - y^2\right), \quad \sigma_{xx}(x,y) = \frac{P(L-x)y}{I}, \quad \sigma_{yy}(x,y) = 0 \tag{2.24}$$

The exact solution for displacements under tensile loading is given by

$$u(x) = \frac{\sigma}{E}x \tag{2.25a}$$

$$v(x,y) = -\nu\frac{\sigma}{E}xy \tag{2.25b}$$

The above exact solutions for displacements are used to compute the error norms, as defined in section 3.1, for shear and tensile loading cases.

Chapter 3

Optimal Numerical Integration

This chapter discusses the proposed two schemes to determine the optimal location of integration points in polygon. One is based on the Frobenius norm and the other is based on the displacement error in infinity norm.

3.1 Global Error Measures

For the purpose of error estimation and convergence studies L_2 norm in interpolation field and energy norm are used. The L_2 norm of displacement error is given by

$$\|\mathbf{u} - \mathbf{u}_h\|_{L_2(\Omega)} = \sqrt{\int_\Omega \left[(\mathbf{u} - \mathbf{u}_h) \cdot (\mathbf{u} - \mathbf{u}_h)\right] d\Omega} \tag{3.1}$$

where $\mathbf{u}_h$ is the numerical solution and $\mathbf{u}$ is the analytical solution, or a reference solution. The energy norm is given by

$$\|\mathbf{u} - \mathbf{u}_h\|_{E(\Omega)} = \sqrt{\int_\Omega \left[(\boldsymbol{\varepsilon} - \boldsymbol{\varepsilon}_h)^T \mathbf{D} (\boldsymbol{\varepsilon} - \boldsymbol{\varepsilon}_h)\right] d\Omega} \tag{3.2}$$

The above norms plotted against the number of nodes to study the convergence as the mesh is refined.

3.2 Determination of Optimal Integration Points

In this section we discuss the methodology employed to obtain the optimal integration points for the quadrilateral, pentagonal and hexagonal elements. As explained earlier, the polygon in physical domain is mapped to non-dimensional coordinates first. For this the integration in equation (2.8) needs to be performed over the reference element domain. This is done by numerically mapping the reference element on to unit-disk by Schwarz-Christoffel conformal mapping and integrating it over this unit-disk. It is impossible to invert the map analytically. Any semi-analytical method of optimizing the Gauss points, as done in case of Gaussian quadrature for isoparametric mapping in quadrilateral element is not feasible in the present case. Therefore an attempt is made to determine the optimal integration points entirely numerically. In conventional isoparametric formulation, Gaussian quadrature gives the exact result for 4-node quadrilateral elements using 2×2 integration rule. Therefore we start only with four integration points in the present method for 4-node quadrilateral element and perform further optimization since we have SC mapping instead of isoparametric mapping on unit-disk. We also show that the present method, with just four integration points gives results comparable to that of isoparametric finite element. This was not possible earlier when a single step mapping using polygon → disk alone with Mid-Point integration scheme was used [20]. This is due to the fact that the Wachspress shape functions are defined over an arbitrary physical polygon, the resulting integrand will have different form for different arbitrary polygonal elements. Later we extend this optimization method to pentagons and hexagons using 5 and 6 integration points, respectively. Figures 2.2c, 2.3c and 2.4c show the location of integration points for quadrilateral, pentagonal and hexagonal elements symmetrically located over the unit-disk.

3.2.1 Optimal integration for polygonal elements: scheme 1

In scheme 1 first the stiffness matrix of the reference element using a known and accurate method, although computationally expensive, is calculated. This solution is referred to

as the reference solution. Now the integration points on unit-disk are placed as shown in figures 2.2c, 2.3c and 2.4c. Initial location of integration points is not important since the location of the integration points is optimized. Let (R, ϕ) be the polar coordinate of an integration point. The stiffness matrix is calculated by the method outlined in section 2.6. The stiffness matrix thus obtained is compared with the stiffness matrix obtained from the reference solution and the error in the stiffness matrix in terms of Frobenius norm of error matrix is calculated. The Frobenius norm of a matrix K is given by

$$\|K\|_F = \sqrt{\sum_{i=1}^{m} \sum_{j=1}^{n} |k_{ij}|^2} \tag{3.3}$$

The error in the stiffness matrix is defined as

$$E_k = \frac{\|K - K_h\|_F}{\|K\|_F} \times 100\ \% \tag{3.4}$$

where K and K_h are the stiffness matrices obtained from reference solution and the proposed solution method with optimised integration points, respectively. Now the values of R and ϕ are varied and error as defined in equation (3.4) is plotted over the entire domain. The value of R and ϕ corresponding to minimum error in E_k gives the optimal integration points. Scheme 1 is applied to quadrilateral (n=4), pentagon (n=5) and hexagon (n=6) and discussed in details in the later sections of this thesis.

3.2.2 Optimal integration for polygonal elements: scheme 2

Scheme 2 is based on minimizing the error in infinity norm of the the displacement. A single element patch test is used to obtain results independent of the mesh. The relative error in infinity norm of displacement is given by

$$E_\infty = \frac{\|\mathbf{u} - \mathbf{u}_h\|_\infty}{\|\mathbf{u}\|_\infty} \tag{3.5}$$

Now from equation (2.7)

$$\mathbf{u} = \mathbf{K}^{-1}\mathbf{f} \tag{3.6a}$$

$$\mathbf{u}_h = {\mathbf{K}_h}^{-1}\mathbf{f} \tag{3.6b}$$

By subtracting equation (3.6b) from equation (3.6a) we get

$$\mathbf{u} - \mathbf{u}_h = \left(\mathbf{K}^{-1} - {\mathbf{K}_h}^{-1}\right)\mathbf{f}$$

Now for the force of unit magnitude ($f = 1$) applied at all nodes (see fig. 3.2, 3.8 and 3.14), one has

$$\mathbf{u} - \mathbf{u}_h = \left(\mathbf{K}^{-1} - {\mathbf{K}_h}^{-1}\right)\mathbf{1} = \sum_j \left({\mathbf{K}_{ij}}^{-1} - {\mathbf{K}_{hij}}^{-1}\right) \tag{3.7}$$

where $\mathbf{1}$ is a vector whose all elements are unity. By taking maximum of absolute values over rows on both sides, we get

$$\max_{1\le i\le n} |\mathbf{u} - \mathbf{u}_h| = \max_{1\le i\le n} \left| \sum_j \left({\mathbf{K}_{ij}}^{-1} - {\mathbf{K}_{hij}}^{-1}\right) \right| \tag{3.8}$$

The left hand side in equation (3.8) is the infinity norm of vector $\mathbf{u} - \mathbf{u}_h$ and the right hand side is the infinity norm of matrix $\mathbf{K}^{-1} - {\mathbf{K}_h}^{-1}$. That is

$$\|\mathbf{u} - \mathbf{u}_h\|_\infty = \left\|\mathbf{K}^{-1} - {\mathbf{K}_h}^{-1}\right\|_\infty \tag{3.9}$$

The relative error in infinity norm is expressed as

$$\frac{\|\mathbf{u} - \mathbf{u}_h\|_\infty}{\|\mathbf{u}\|_\infty} = \frac{\left\|\mathbf{K}^{-1} - {\mathbf{K}_h}^{-1}\right\|_\infty}{\|\mathbf{K}^{-1}\|_\infty} = \frac{\left\|{\mathbf{K}_h}^{-1} - \mathbf{K}^{-1}\right\|_\infty}{\|\mathbf{K}^{-1}\|_\infty} \tag{3.10}$$

The right most expression in equation (3.10) gives the relative error in infinity norm of displacement in terms of stiffness matrices. This error in infinity norm of displacement vs. R and ϕ is plotted and the values of R and ϕ corresponding to minimum error give the optimal integration points. Scheme 2 is applied to quadrilateral (n=4), pentagon

(n=5) and hexagon (n=6) as discussed in the later sections of this thesis.

Now we further investigate the upper bound of error in infinity norm of displacement as given by equation (3.10). We frequently use norms to quantify the effect of perturbations. As an illustration of this, let us quantify the change in $\mathbf{K}^{-1}$ as a function of change in $\mathbf{K}$. Let us use error in stiffness matrix $\mathbf{E} = \mathbf{K}_h - \mathbf{K}$ as a perturbation in stiffness matrix $\mathbf{K}$. Now if $\mathbf{K}$ is non-singular and $\mathbf{r} \equiv \|\mathbf{K^{-1}E}\|_\infty < \mathbf{1}$, then $\mathbf{K} + \mathbf{E}$ is nonsingular and from the theorem given in Ref. [41]

$$\left\|(\mathbf{K}+\mathbf{E})^{-1} - \mathbf{K}^{-1}\right\|_\infty \leq \frac{\|\mathbf{E}\|_\infty \|\mathbf{K}^{-1}\|_\infty^2}{1-\mathbf{r}} \tag{3.11}$$

on rearranging the terms we get

$$\frac{\left\|(\mathbf{K}+\mathbf{E})^{-1} - \mathbf{K}^{-1}\right\|_\infty}{\|\mathbf{K}^{-1}\|_\infty} \leq \frac{\|\mathbf{E}\|_\infty \|\mathbf{K}^{-1}\|_\infty}{1-\mathbf{r}} \tag{3.12}$$

The left hand sides in equation (3.12) is the error in infinity norm of the displacement as given by equation (3.10) which involves computation of several matrix inversions. Its upper bound (for $E < 100\%$) can be computed more accurately since it involves computation of K^{-1} only once. The above gives good reliability in computing infinity norm error.

3.3 Analysis and Comparison of Results: Quadrilaterals (n=4)

The reference element is shown in Figure 2.2b. Now let us write the Wachspress interpolation functions for a polygon (n=4) when it degenerates to the reference quadrilateral. By using equations (2.17) and (2.18) and substituting coordinates of the vertices the shape functions at any generic point $p(\bar{\xi}, \bar{\eta})$ within the element are obtained for reference quadrilateral. The main steps are given below. Quantities W_i in equation (2.17a)

become

$$W_1 = \frac{2}{(1+\bar{\xi})(1+\bar{\eta})}, \quad W_2 = \frac{2}{(1-\bar{\xi})(1+\bar{\eta})} \tag{3.13a}$$

$$W_3 = \frac{2}{(1-\bar{\xi})(1-\bar{\eta})}, \quad W_4 = \frac{2}{(1+\bar{\xi})(1-\bar{\eta})} \tag{3.13b}$$

$$\sum_{i=1}^{4} W_i = W_1 + W_2 + W_3 + W_4 = \frac{8}{(1-\bar{\xi}^2)(1-\bar{\eta}^2)} \tag{3.14}$$

Now based on equation (2.17a), the shape functions are given by

$$N_i = \frac{W_i}{\sum_{i=1}^{4} W_i} \tag{3.15}$$

Substituting W_i from eqs. (3.13) and (3.14), we get

$$N_1 = \frac{(1-\bar{\xi})(1-\bar{\eta})}{4}, \quad N_2 = \frac{(1+\bar{\xi})(1-\bar{\eta})}{4} \tag{3.16a}$$

$$N_3 = \frac{(1+\bar{\xi})(1+\bar{\eta})}{4}, \quad N_4 = \frac{(1-\bar{\xi})(1+\bar{\eta})}{4} \tag{3.16b}$$

It is observed that the shape functions obtained in equation (3.16) are indeed the bilinear shape functions in of the 4-node isoparametric quadrilateral. Therefore we start with the same 2×2 Gauss integration points, which are optimal in isoparametric formulation. We then show that since we have SC mapping, these points are not the optimal points in the present case and later on we obtain the optimal integration points for the same by the two different schemes explained in sec. 3.2.1 and sec. 3.2.2.

3.3.1 Scheme 1 applied to quadrilaterals (n=4)

The integration points for quadrilaterals for 2×2 Gauss integration rules are shown in figure 2.2b and denoted by "×" markers. As discussed previously, we compute the error in Frobenius norm of stiffness matrix. An error of 28 % is found with the present 2×2 integration points. Hence these points are not optimal in the present case of SC mapping.

We now represent integration points in polar coordinates r and θ. Then we vary the angle θ in small steps keeping the radius r constant at value equal to the radial distance of integration points in 2×2 Gauss rule. The coordinates of the integration points in the Cartesian coordinate system are calculated as

$$\bar{\xi}_i = r\cos\left(\theta + \frac{\pi}{2}(i-1)\right) \;;\; \bar{\eta}_i = r\sin\left(\theta + \frac{\pi}{2}(i-1)\right) \tag{3.17}$$

for the i^{th} integration point, where $1 \leq i \leq 4$. The stiffness matrix from an isoparametric

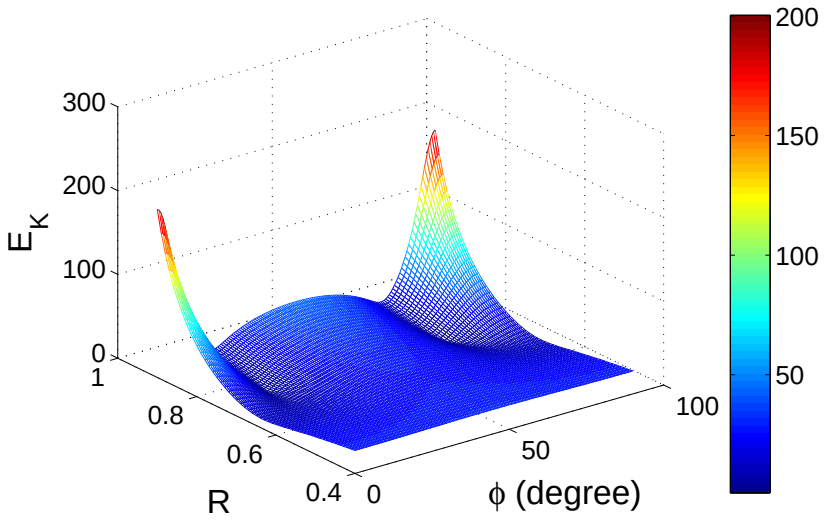

Figure 3.1: Error in Frobenius norm vs. coordinates (R, ϕ) of integration points on unit circle for 4-node quadrilateral element.

formulation is used as reference solution. It is apparent that for every point $p(\bar{\xi}, \bar{\eta})$ in the quadrilateral there is a corresponding point $p(\xi, \eta)$ in the unit-disk. These points on the unit-disk are represented by R and ϕ in polar coordinates. The error in Frobenius norm vs. R and ϕ is plotted in Figure 3.1. The values of R and ϕ and hence r and θ corresponding to minimum error are given in table 3.1. These optimal integration points are shown in figure 2.2b and denoted by "$\diamond$" markers. A careful observation shows that the radial location of these integration points is the same as in 2×2 Gauss integration rules but they are now rotated by an angle of 18.086559^o. In fact rotation of 2×2 Gauss points by an angle of -18.086559^o also gives the same result.

Table 3.1: Optimal coordinate of integration points for 4-node quadrilateral element.

	In quadrilateral domain (fig. 2.2b)	In unit-disk domain (fig. 2.2c)
Min. error in Frobenius norm	$8 \times 10^{-4}\%$	$8 \times 10^{-4}\%$
$Radius_{opt}$	0.816496	0.749209
$Angle_{opt}$	63.086559^o	16.306493^o

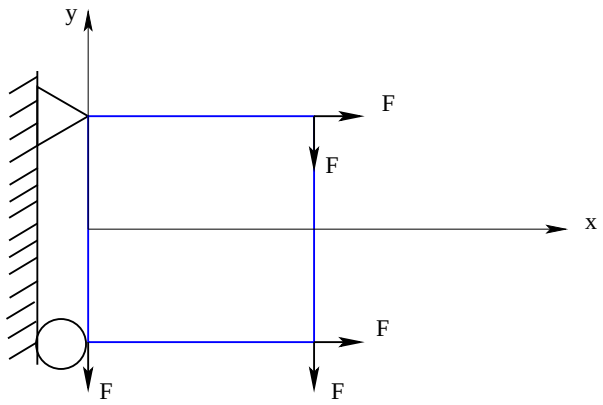

Figure 3.2: FE model with boundary conditions for scheme 2 based optimization for quadrilateral element.

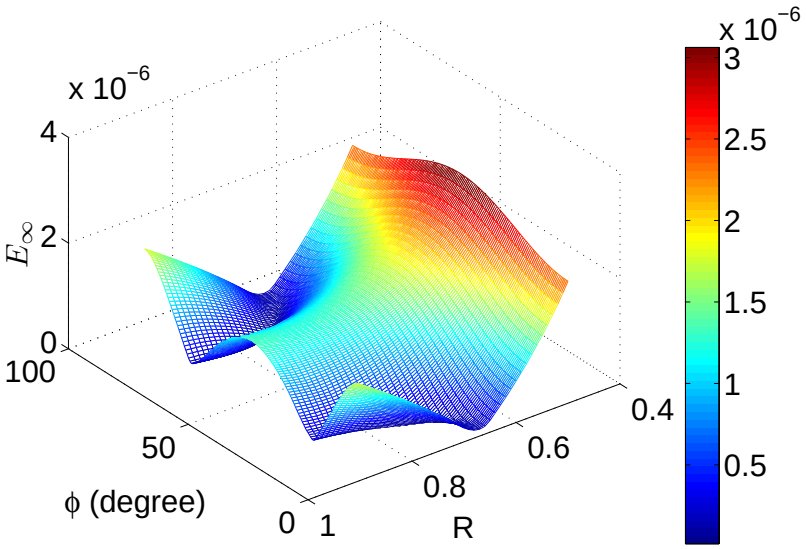

Figure 3.3: Error in infinity norm of u vs. coordinates (R, ϕ) of integration points on unit circle for 4-node quadrilateral element.

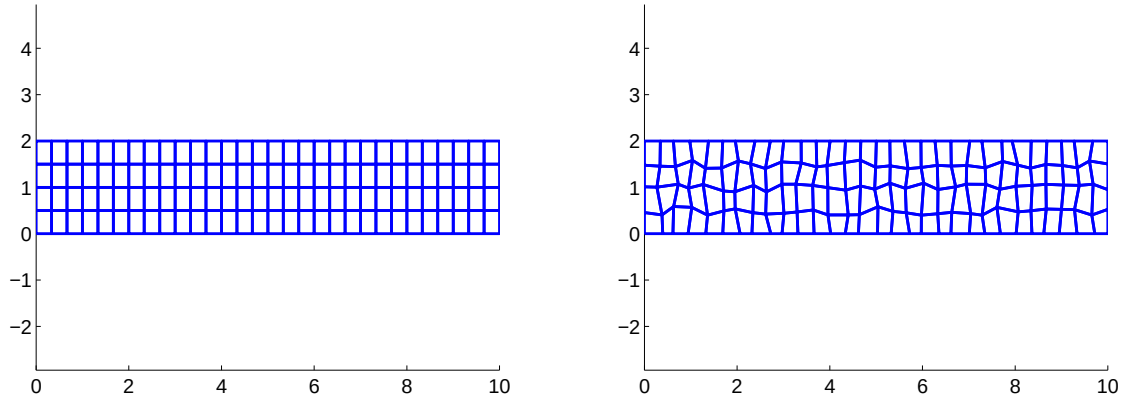

Figure 3.4: (a) Structured mesh and (b) unstructured mesh with quadrilateral elements.

3.3.2 Scheme 2 applied to quadrilaterals (n=4)

Figure 3.2 shows the finite element model with essential and natural boundary conditions used for optimization using scheme 2 for 4-node quadrilateral element. The error in infinity norm of the displacement as given by equation (3.10) vs. R and ϕ is plotted in figure 3.3. The integration points thus obtained by scheme 2 for quadrilateral are found to be the same as those obtained by scheme 1 (table 3.1).

Figure 3.4 shows a typical structured mesh and an unstructured mesh with 4-node quadrilateral elements. Results obtained based on the above optimal integration points are shown in figures 3.5 and 3.6. Convergence in strain energy against the number of nodes for structured and unstructured mesh under pure tensile loading case is shown in figures 3.5a and 3.5c, respectively. The error in strain energy for SC mid-point method is 7 % with about 200 nodes whereas in case of the present method the error in strain energy is less than 0.001 % with only 9 nodes for structured quadrilateral mesh. Similar results are observed for unstructured quadrilateral mesh too. Convergence in strain energy against the number of nodes for structured and unstructured mesh under pure shear loading case is shown in figures 3.5b and 3.5d, respectively. Convergence rate in energy norm (H_1) is shown in figure 3.5 (in inset) for various cases. Please refer to table 3.2 for comparison of convergence rate for different schemes. Negative values of

Table 3.2: Comparison of convergence rate (least square fit) in energy norm for structured (S) and unstructured (US) 4-node quadrilateral mesh.

Method	Convergence rate in energy norm for shear loading (S/US)	Convergence rate in energy norm for tensile loading (S/US)	Monotonic convergence (S/US)
SC mid-point	1.2/0.6	1.5/1.2	No/No
Scheme 1 & 2	3.1/2.7	0/0	Yes/Yes

convergence rate indicate a diverging solution.

Convergence in relative error in L_2 norm of displacement is plotted in figure 3.6. In this case too the present method is much superior to SC mid-point method. For the tensile loading case the error in L_2 norm for the present method with only 9 nodes is of the order of 10^{-7} and 10^{-2} for structured and unstructured meshes, respectively (figures 3.6a and 3.6c). Whereas the order of error in L_2 norm for the SC mid-point method even with 200 nodes is 10^{-1} for both structured and unstructured mesh. For the case of shear loading the error in L_2 norm is two order lower in case of the present method than the error in case of the SC mid-point method with 200 nodes (see figures 3.6b and 3.6d).

3.4 Analysis and Comparison of Results: Pentagons (n=5)

For pentagons there is no established optimal integration rule or isoparametric mapping known till date. Therefore we define the integration points in the unit-disk directly. Moreover the initial location of integration points is not important as we will be optimizing for the integration points. Since only 4 integration points were needed in the case of 4-node quadrilateral elements, intuitively we choose just 5 integration points for a 5-node pentagon. The scheme of placement of integration points on the unit-disk is shown in figure 2.3c. The coordinates of the integration points in Cartesian coordinate coordinate system are calculated from R and ϕ as

$$\xi_i = R\cos\left(\phi + \frac{2\pi}{5}(i-1)\right) \; ; \; \eta_i = R\sin\left(\phi + \frac{2\pi}{5}(i-1)\right) \tag{3.18}$$

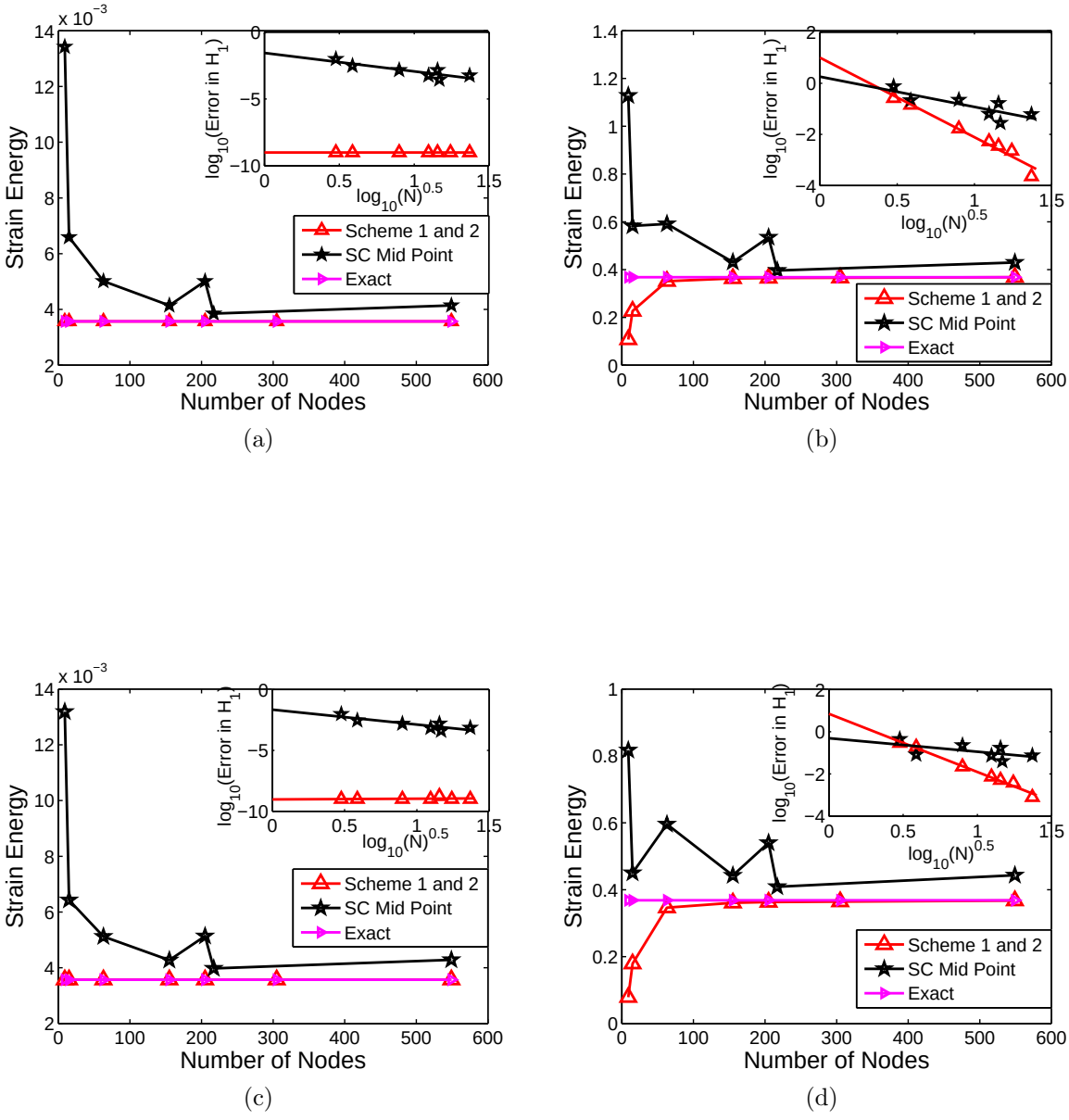

Figure 3.5: Error in energy norm vs. number of nodes (4-node quadrilateral mesh). Convergence rate in energy norm (H_1) (in inset) (a) Structured mesh (Tension). (b) Structured mesh (Shear). (c) Unstructured mesh (Tension). (d) Unstructured mesh (Shear).

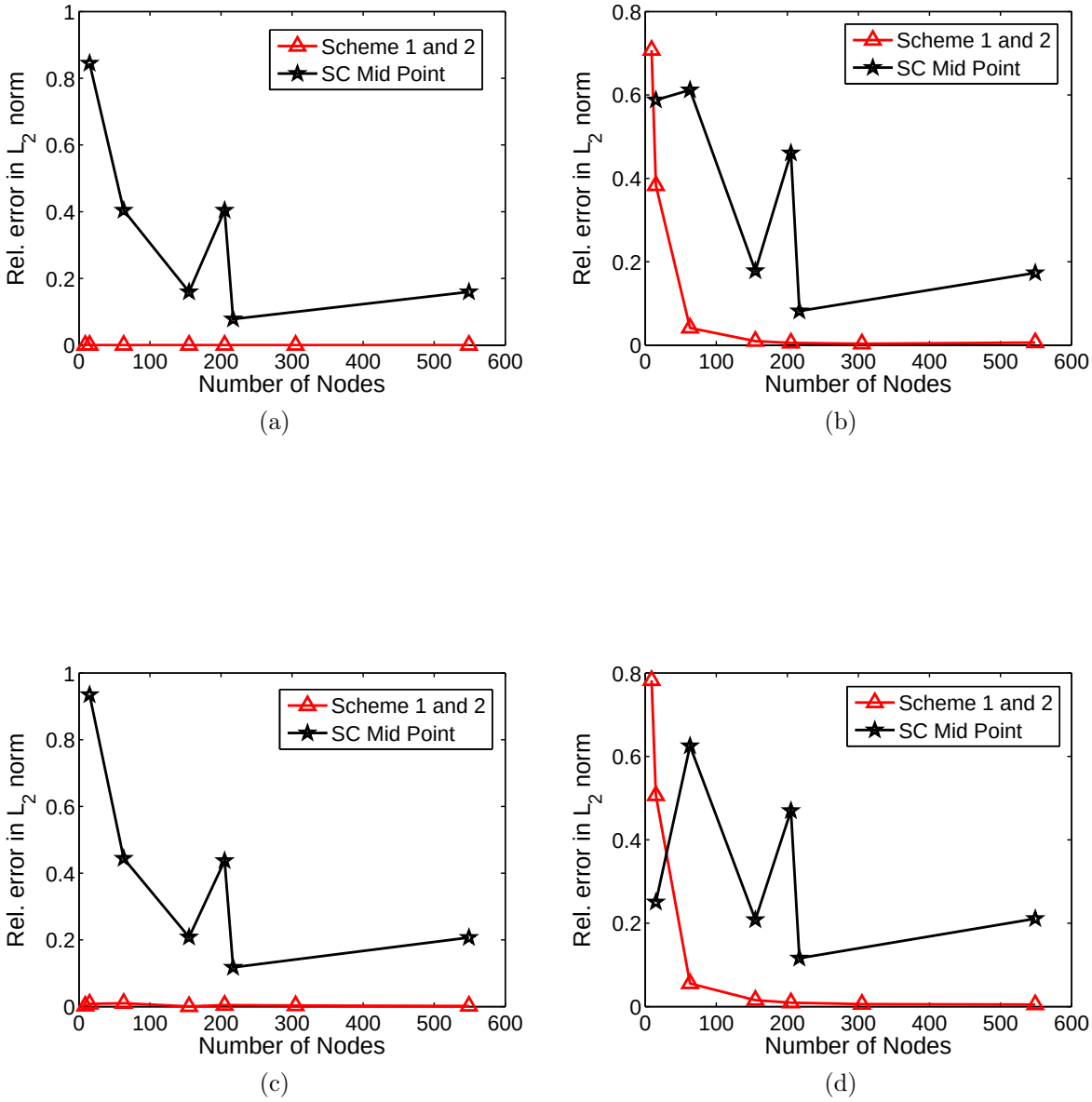

Figure 3.6: Error in L_2 norm vs. number of nodes (4-node quadrilateral mesh). (a) Structured mesh (Tension). (b) Structured mesh (Shear). (c) Unstructured mesh (Tension). (d) Unstructured mesh (Shear).

for the i^{th} integration point, where $1 \leq i \leq 5$.

3.4.1 Scheme 1 applied to pentagons (n=5)

The triangulation method or the method proposed in Ref. [35] could be used to obtain the reference solution for a pentagonal element. We use the triangulation method, as discussed in section 2.4, with a large number of integration points to construct a reference solution. We use the integration rule given by Dunavant [42] with 79 integration points per triangle, where five symmetrically placed triangles represent the pentagon. This rule can be used to integrate polynomials of degree 20 exactly.

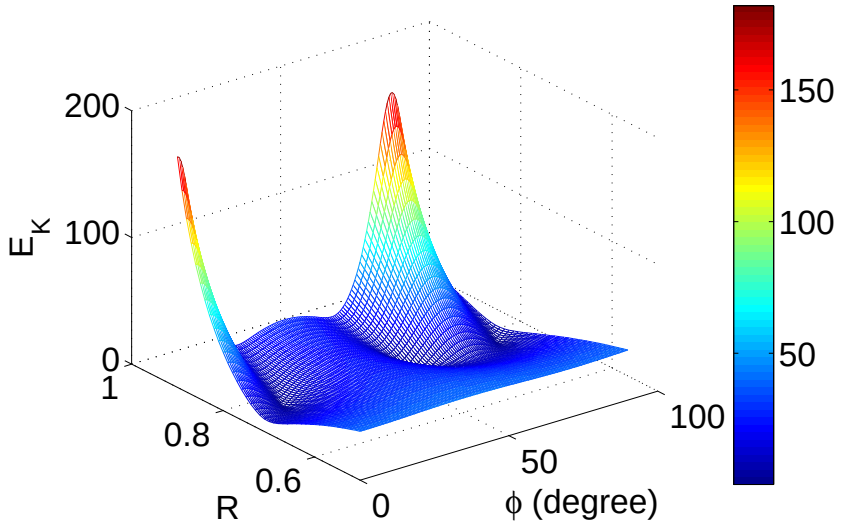

Figure 3.7: Error in Frobenius norm of u vs. coordinates (R, ϕ) of integration points on unit circle for 5-node pentagonal element.

The error in Frobenius norm vs. R and ϕ is plotted in Figure 3.7. The values of R and ϕ corresponding to minimum error are given in table 3.3. We notice that the error in Frobenius norm in the stiffness matrix obtained using only 5 optimal integration points with SC mapping is very small when compared with the reference solution which uses 395 integration points in the pentagonal element.

Table 3.3: Optimal coordinate of integration points for 5-node pentagonal element

	Scheme 1	Scheme 2
Min. error	0.1506 % in E_K	5×10^{-9} in E_∞
R_{opt}	0.761	0.761
ϕ_{opt}	57.817^o	57.817^o

3.4.2 Scheme 2 applied to pentagons (n=5)

Figure 3.8 shows the finite element model with essential and natural boundary conditions used for optimization using scheme 2 for a pentagonal element. We use the same method to obtain the reference solution as used in scheme 1. The error in the infinity norm of the displacement as given by equation (3.10) vs. R and ϕ is plotted in figure 3.9. The values of R and ϕ corresponding to the minimum error are the coordinate of the optimal integration points. The optimal integration points obtained are given in table 3.3 and interestingly they are the same as those obtained by scheme 1 (down to three decimal places). Since it is not possible to obtain a structured pentagonal mesh in a rectangular

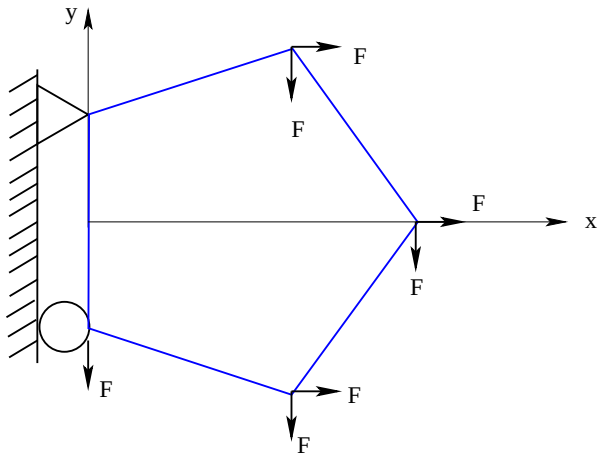

Figure 3.8: FE model with boundary conditions for scheme 2 based optimization for pentagonal element.

geometry, therefore only an unstructured mesh (Figure 3.10) is used for comparison of results. Results obtained from the above optimal integration points are plotted in figures 3.11 and 3.12. Convergence in strain energy versus number of nodes for pure tensile loading is shown in figure 3.11a. There is an error of 16 % in strain energy when SC

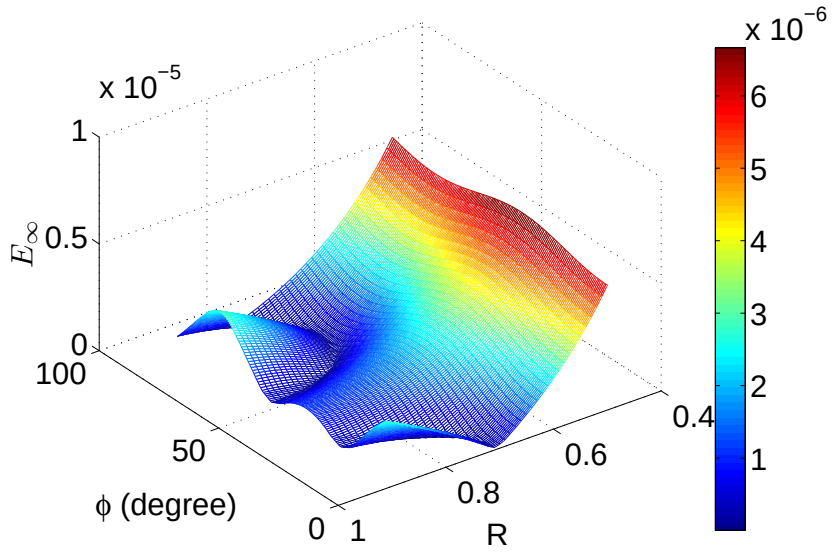

Figure 3.9: Error in infinity norm of u vs. coordinates (R, ϕ) of integration points on unit circle for 5-node pentagonal element.

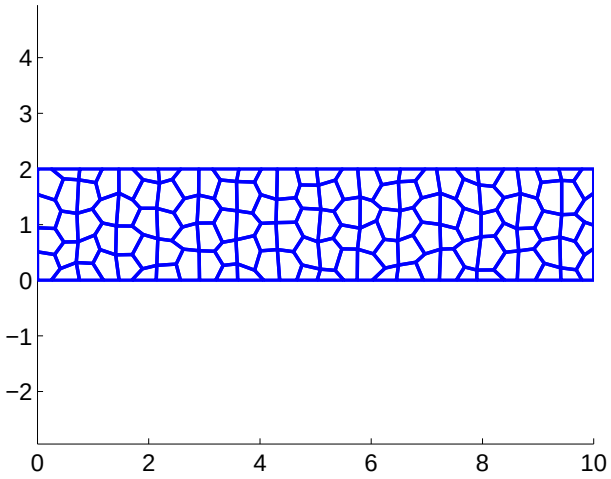

Figure 3.10: An unstructured mesh with pentagonal elements.

Table 3.4: Comparison of convergence rate (least square fit) in energy norm for 5-node pentagonal mesh.

Method	Convergence rate in energy norm for shear loading	Convergence rate in energy norm for tensile loading	Monotonic convergence
SC mid-point	0	0.24	No
Scheme 1 & 2	2.3	-0.5	Yes

mid-point method is used with 119 nodes, whereas in case of the present method the error in strain energy is less than 0.001 % with only 22 nodes. Figure 3.11b shows the convergence in strain energy versus number of nodes for pure shear loading. The present method with 5 optimal integration points needs around 400 nodes to achieve an error less than 1 % whereas the error in case of the SC mid-point method with same number of nodes is 16 %. Convergence rate in energy norm (H_1) is shown in figure 3.11 (in inset) for various cases. The solution seems to be slightly diverging in case of the present method for tensile loading case. However the error in energy norm is less than 0.045% even for the largest value of error. Table 3.4 shows a comparison of convergence rate for different schemes.

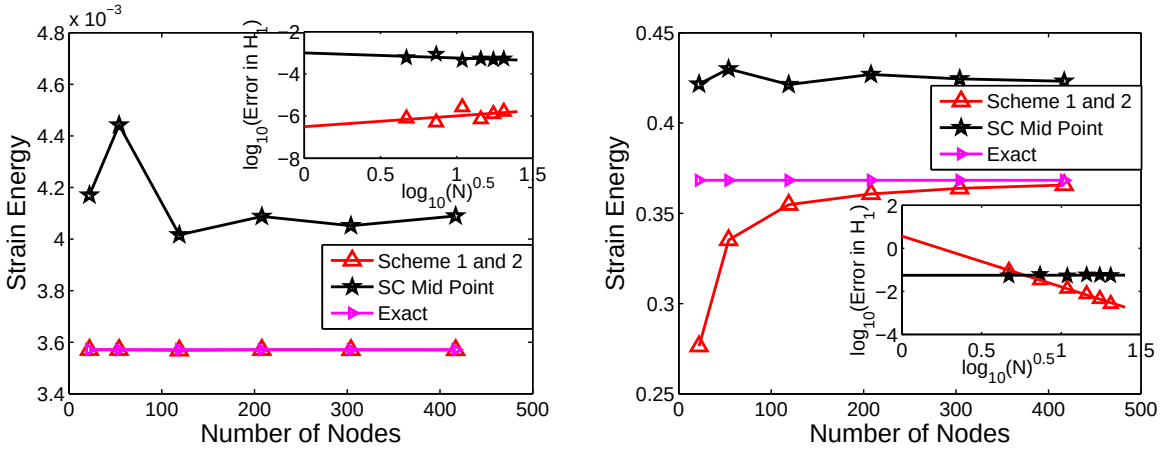

Figure 3.11: Error in energy norm vs. number of nodes (5-node pentagonal mesh). Convergence rate in energy norm (H_1) (in inset) (a) Unstructured mesh (Tension). (b) Unstructured mesh (Shear).

Convergence in relative error in L_2 norm of displacement is plotted in figure 3.12. In

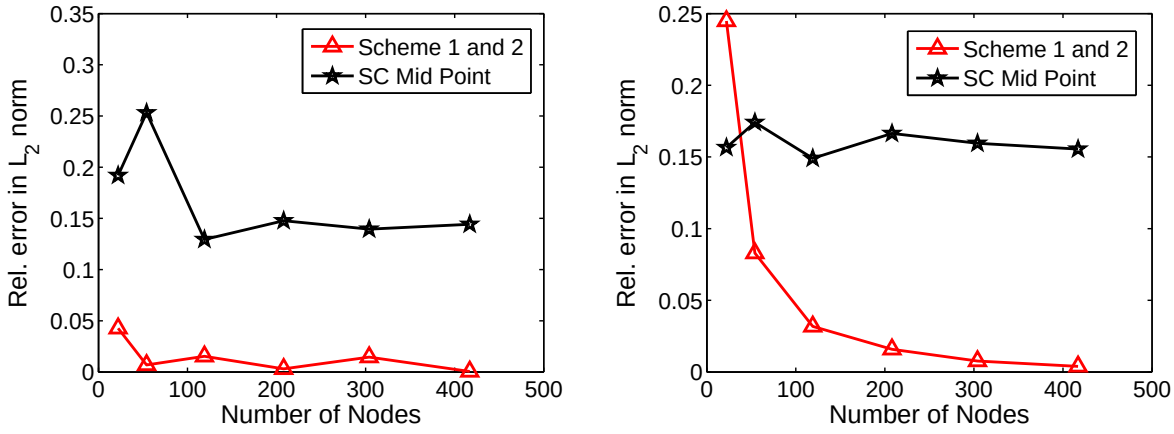

(a) (b)

Figure 3.12: Error in L_2 norm vs. number of nodes (5-node pentagonal mesh). (a) Unstructured mesh (Tension). (b) Unstructured mesh (Shear).

this case too the present method is much superior to SC mid-point method. In tensile loading case (figure 3.12a), results show that there is an error of 0.15 % in L_2 norm in case of the present method with around 100 nodes. Whereas the SC mid-point method has an error of 1.3 % with the same number of nodes. For the case of shear loading (figure 3.12b) the the error in L_2 norm with the present method is 0.39 % with around 400 nodes whereas the SC mid-point method gives an error of 15 % with same number of nodes.

3.5 Analysis and Comparison of Results: Hexagons (n=6)

As pointed out in case of pentagons, there is no established optimal integration rule for $n > 4$. Therefore we define the integration points in the unit-disk as done in case of pentagons. Similarly, here also initial location of integration point is unimportant since we will be optimizing their coordinates. Intuitively we choose 6 integration points for a 6-node hexagon (n=6). The scheme for placement of integration points is shown in figure 2.4c. The coordinates of the integration points in Cartesian coordinate system are

calculated as

$$\xi_i = R\cos\left(\phi + \frac{2\pi}{6}(i-1)\right) \; ; \; \eta_i = R\sin\left(\phi + \frac{2\pi}{6}(i-1)\right) \tag{3.19}$$

for the i^{th} integration point, where $1 \leq i \leq 6$.

3.5.1 Scheme 1 applied to hexagons (n=6)

The triangulation method or the method proposed in Ref. [35] could be used to obtain the reference solution for a hexagonal element. We use the triangulation method, as discussed in section 2.4, with a large number of integration points to construct a reference solution. Here we use integration rule given by Dunavant [42] with 79 integration points per triangle as done in the case of pentagons.

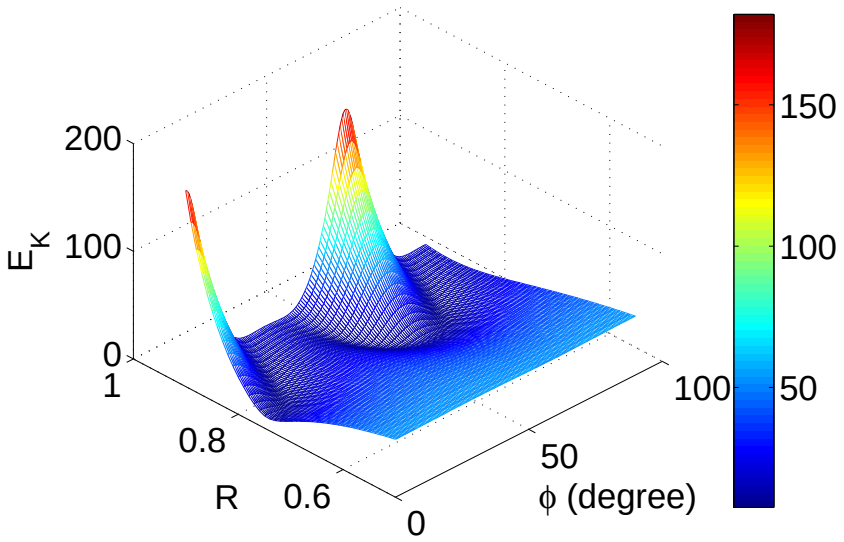

Figure 3.13: Error in Frobenius norm of u vs. coordinates (R, ϕ) of integration points on unit circle for 6-node hexagonal element.

The error in the Frobenius norm vs. R and ϕ is plotted in Figure 3.13. The values of R and ϕ corresponding to the minimum error are given in table 3.5. We notice that the error in the Frobenius norm of stiffness matrix obtained using just 6 optimal integration points with SC mapping is very small when compared with the reference solution which

Table 3.5: Optimal coordinate of integration points for 6-node hexagonal element.

	Scheme 1 (fig. 2.4b)	Scheme 2
Min. error	7.6089 % in E_K	2×10^{-7} in E_∞
R_{opt}	0.788	0.797
ϕ_{opt}	46.719^o	46.811^o

uses 474 integration points element.

3.5.2 Scheme 2 applied to hexagons (n=6)

Figure 3.14 shows the finite element model with essential and natural boundary conditions used for optimization using scheme 2 for a hexagonal element. We use the same method for getting reference solution as used in scheme 1. The error in the infinity norm of displacement as given by equation (3.10) vs. R and ϕ is plotted in figure 3.15. The values of R and ϕ corresponding to minimum error are given in table 3.5.

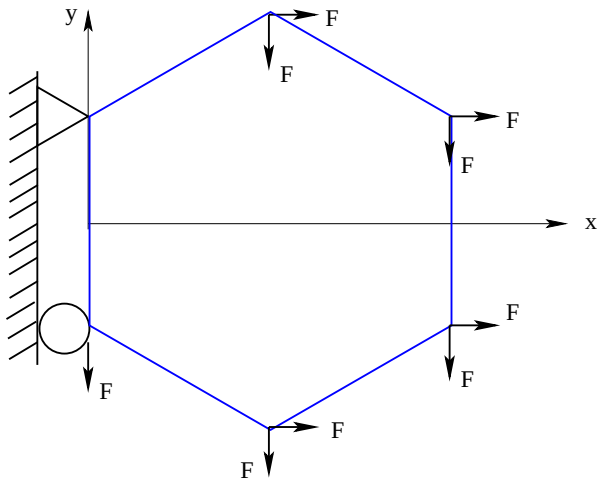

Figure 3.14: FE model with boundary conditions for scheme 2 based optimization for hexagonal element.

Figure 3.16 shows a structured mesh and an unstructured mesh with 6-node hexagonal elements. Results obtained using the optimal integration points are shown in figures 3.17 and 3.18. Convergence in strain energy versus the number of nodes for structured and unstructured mesh under pure tension are shown in figures 3.17a and 3.17c, respectively. It is clear from the figures that strain energy varies by less than 0.25 % between mesh 1

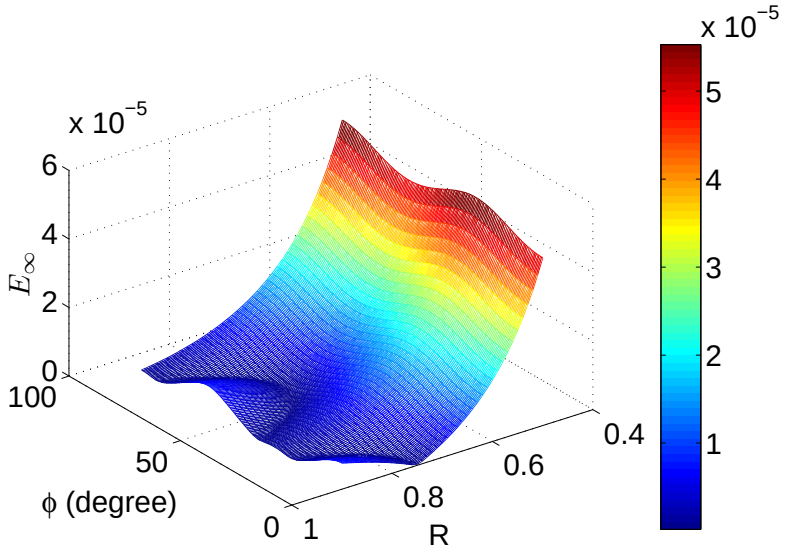

Figure 3.15: Error in infinity norm of u vs. coordinates (R, ϕ) of integration points on unit circle for 6-node hexagonal element.

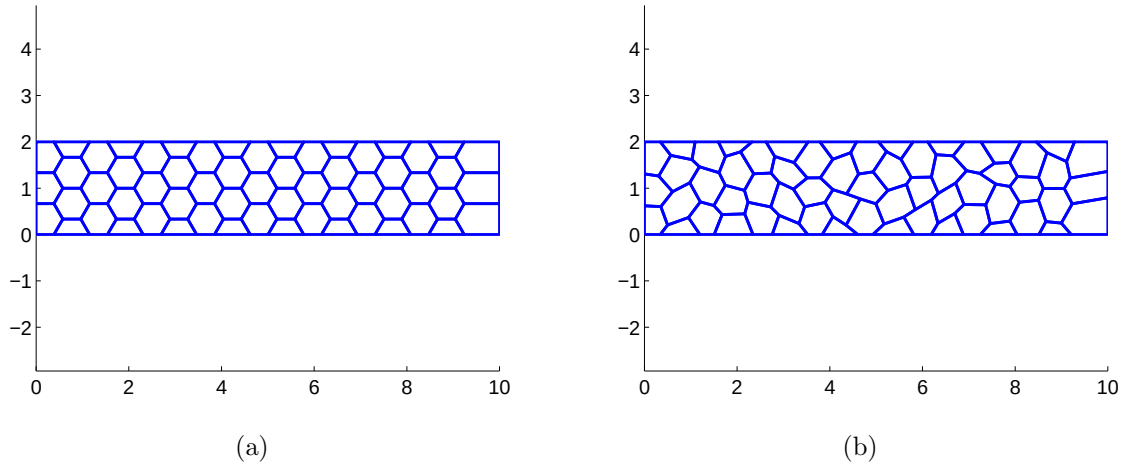

Figure 3.16: (a) Structured mesh and (b) unstructured mesh with hexagonal elements.

Table 3.6: Comparison of convergence rate (least square fit) in energy norm for structured (S) and unstructured (US) 6-node hexagonal mesh.

Method	Convergence rate in energy norm for shear loading (S/US)	Convergence rate in energy norm for tensile loading (S/US)	Monotonic convergence (S/US)
SC mid-point	-0.4/-0.8	0.5/0.6	No/No
Scheme 1	3.6/3.1	-1/-1	Yes/Yes
Scheme 2	2.8/2.7	-1/-1	Yes/Yes

and mesh 2 for the present method with 6 optimal integration points. On the other hand the SC mid-point method with the same number of integration points does not converge to the exact value even for 450 nodes for which the error is still 9.8 %. Figure 3.17b shows the convegence curves under shear loading case for hexagonal structured mesh. Although the convergence rate with the present method is slower but finally it converges at 300 nodes with an error of less than 1 %. Whereas in the case of SC mid-point method with 6 integration points there is a saturation (locking) in strain energy with about 50 nodes for an error of 14 % but it never converges. Similar observations are made for the structured hexagonal mesh too (3.17d). Convergence rate in energy norm (H_1) is shown in figure 3.17 (in inset) for various cases. The solution seems to be slightly diverging in case of the present method for tensile loading case. However the error in energy norm is $\leq 1.2\%$ even for the largest value of error. Table 3.6 shows a comparison of convergence rate for different schemes.

Convergence in relative error in L_2 norm of displacement is plotted in figure 3.18. Here also the convergence curves show similar trends as observed in case of convergence in strain energy. It is also seen that the two schemes give almost similar results due to the fact that the difference in the coordinates of integration points is small.

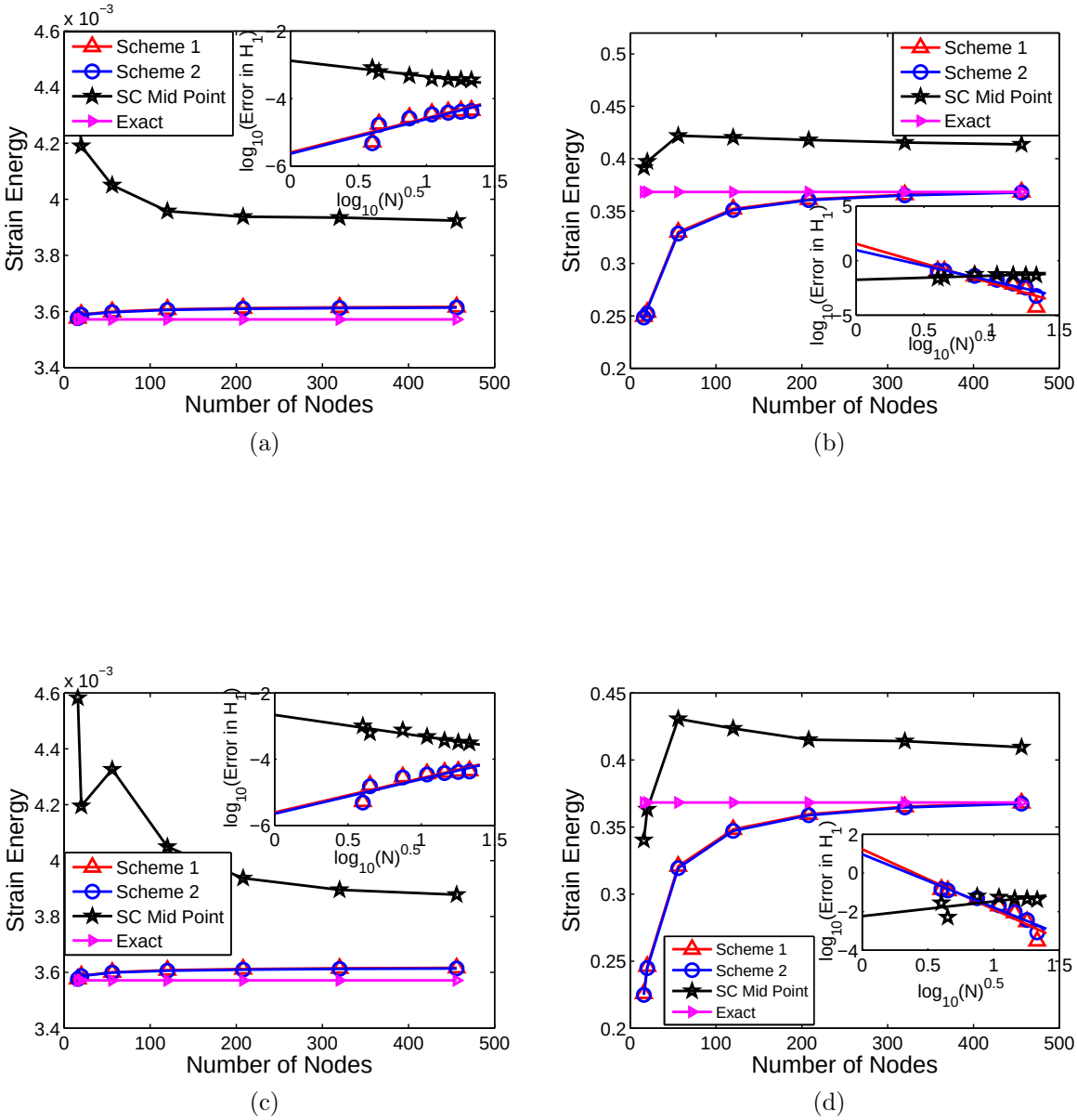

Figure 3.17: Error in energy norm vs. number of nodes (6-node hexagonal mesh). Convergence rate in energy norm (H_1) (in inset). (a) Structured mesh (Tension). (b) Structured mesh (Shear). (c) Unstructured mesh (Tension). (d) Unstructured mesh (Shear).

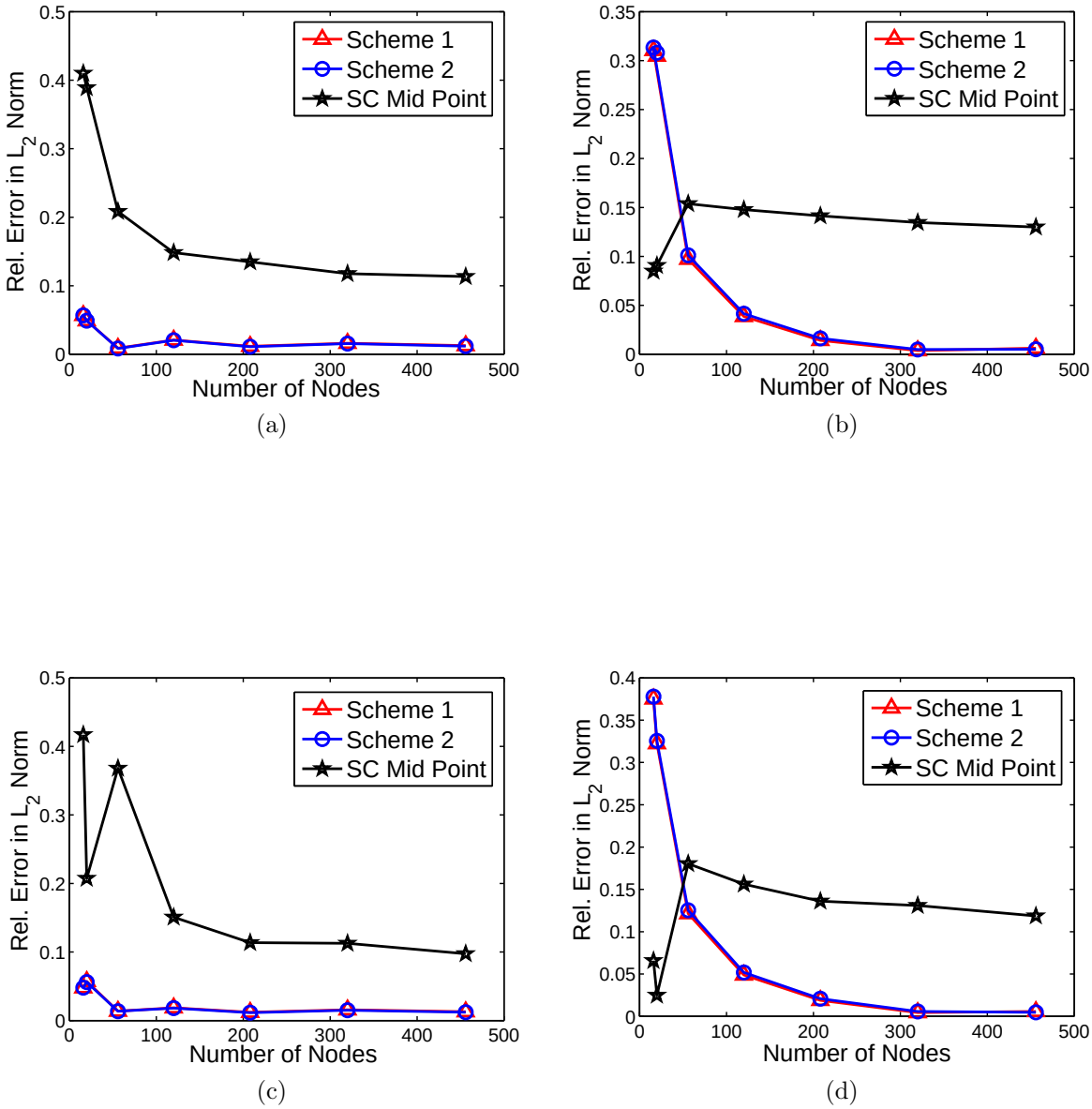

Figure 3.18: Error in L_2 norm vs. number of nodes (6-node hexagonal mesh). (a) Structured mesh (Tension). (b) Structured mesh (Shear). (c) Unstructured mesh (Tension). (d) Unstructured mesh (Shear).

Chapter 4

Extended Finite Element Method: Formulation

4.1 Governing Equations and Weak Form

The governing equilibrium equations for a 2D static elasticity problem defined in the domain Ω bounded by Γ and $\Gamma = \Gamma_u \cup \Gamma_t \cup \Gamma_c$ (fig. 4.1), can be expressed as

$$\nabla_s^{\mathrm{T}} \boldsymbol{\sigma} + \mathbf{b} = \mathbf{0} \quad \text{in } \Omega \tag{4.1}$$

where $\mathbf{0}$ is a null vector, $\boldsymbol{\sigma}$ is the stress tensor and b is the vector of external forces.

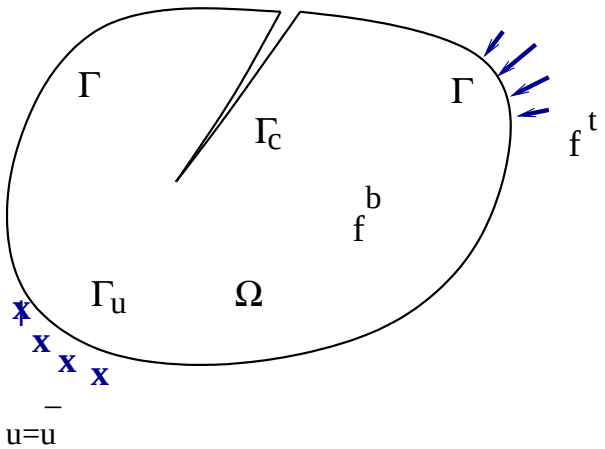

Figure 4.1: A body in a state of elastostatic equilibrium.

The following are the prescribed boundary conditions

$$\mathbf{u} = \overline{\mathbf{u}} \ \ in \ \ \Gamma_u \tag{4.2a}$$

$$\mathbf{n}^T\boldsymbol{\sigma} = \overline{\mathbf{t}} \ \ on \ \ \Gamma_t \tag{4.2b}$$

$$\mathbf{n}^T\boldsymbol{\sigma} = \mathbf{0} \ \ on \ \ \Gamma_c \tag{4.2c}$$

where $\overline{\mathbf{u}} = (\overline{u}_x, \overline{u}_y)^T$ is the prescribed displacement vector on the essential boundary Γ_u; $\mathbf{t} = (\overline{t}_x, \overline{t}_y)^T$ is the prescribed traction vector on the natural boundary Γ_t and Γ_c is the traction free boundary condition at crack all faces; $\mathbf{n}$ is the unit outward normal vector. The discrete version of the weak form for this problem are obtained using Galerkin approach as

$$\int_\Omega (\bigtriangledown_s \delta\mathbf{u})^T \mathbb{D} (\bigtriangledown_s \mathbf{u}) d\Omega - \int_\Gamma (\delta\mathbf{u}^T)\mathbf{b} d\Omega - \int_\Gamma (\delta\mathbf{u})^T \overline{\mathbf{t}} d\Gamma = 0 \tag{4.3}$$

where $\mathbf{u}$ and $\delta\mathbf{u}$ are the test functions that belong to admissible functions from Sobolev space and $\mathbb{D}$ is the constitutive matrix. The extended finite element method uses the following trial function $\mathbf{u}_h(\mathbf{x})$ and the test function $\delta\mathbf{u}_h(\mathbf{x})$:

$$\mathbf{u}_h(\mathbf{x}) = \sum_{i=1}^{N_P} \mathbf{N}_i(\mathbf{X})\mathbf{u}_i + \sum_{j=1}^{m} \mathbf{N}_k(\mathbf{X})\psi(\mathbf{X})\mathbf{a}_k \tag{4.4a}$$

$$\delta\mathbf{u}_h(\mathbf{x}) = \sum_{i=1}^{N_P} \mathbf{N}_i(\mathbf{X})\delta\mathbf{u}_i + \sum_{j=1}^{m} \mathbf{N}_k(\mathbf{X})\psi(\mathbf{X})\delta\mathbf{a}_k + \sum_{j=1}^{m} \mathbf{N}_k(\mathbf{X})\delta\psi(\mathbf{X})\mathbf{a}_k \tag{4.4b}$$

where N_P is the total number of nodes in the mesh, m is the number of enriched nodes, $\mathbf{a}_k$ is the set of degrees of freedom added to the standard finite element modal degrees of freedom and $\psi(\mathbf{X})$ is the discontinuous enrichment function. By substituting the approximations $\mathbf{u}^h$ and $\delta\mathbf{u}^h$ into the weak form and invoking the arbitrariness of virtual nodal displacements, equation (4.3) yields the standard discretized algebraic system of equations:

$$\mathbf{K}\mathbf{u} = \mathbf{f} \tag{4.5}$$

with the stiffness matrix given by

$$\mathbf{K_{ij}^{e}} = \begin{bmatrix} \mathbf{K_{ij}^{uu}} & \mathbf{K_{ij}^{ua}} & \mathbf{K_{ij}^{uc}} \\ \mathbf{K_{ij}^{au}} & \mathbf{K_{ij}^{aa}} & \mathbf{K_{ij}^{ac}} \\ \mathbf{K_{ij}^{cu}} & \mathbf{K_{ij}^{ca}} & \mathbf{K_{ij}^{cc}} \end{bmatrix} \tag{4.6}$$

and the load vector by

$$\mathbf{f_i} = \begin{bmatrix} \mathbf{f_i^u} & \mathbf{f_i^a} & \mathbf{f_i^{c1}} & \mathbf{f_i^{c2}} & \mathbf{f_i^{c3}} & \mathbf{f_i^{c4}} \end{bmatrix}^T \tag{4.7}$$

$\mathbf{u}$ is a vector of nodal parameters and given by

$$\mathbf{u^h} = \begin{bmatrix} \mathbf{u} & \mathbf{a} & \mathbf{c1} & \mathbf{c2} & \mathbf{c3} & \mathbf{c4} \end{bmatrix}^T \tag{4.8}$$

4.2 Crack Modeling Using Discontinuous Enrichment

The main idea in Partition of Unity Methods is to extend the approximation basis by a set of enrichment functions that are chosen based on the local behavior of the problem. For the case of linear elastic fracture mechanics, two sets of functions are used: a Heaviside jump function to capture the jump across the crack faces and asymptotic branch functions that span the 2D asymptotic crack tip fields. The enriched approximation for fracture mechanics problems takes the form [4]:

$$\mathbf{u^h}(\mathbf{x}) = \sum_{i \in I} N_i(\mathbf{x})\, \mathbf{u_i} + \sum_{j \in J} N_j(\mathbf{x})\, H(\mathbf{x})\, \mathbf{a_j} + \sum_{j \in K} N_j(\mathbf{x}) \sum_{\alpha=1}^{4} \psi_\alpha(\mathbf{x})\, \mathbf{b_{k\alpha}} \tag{4.9}$$

$N_i(x)$ is the polygonal basis function of node i. Where $\mathbf{a_j}$ and $\mathbf{b_{k\alpha}}$ are enrichment nodal degrees of freedom corresponding to the Heaviside function H and the near-tip functions ψ_α, respectively. Signed distance function for Heaviside function H is given by

$$H(\xi) = \begin{cases} 1 & \forall \xi > 0 \\ -1 & \forall \xi < 0 \end{cases} \tag{4.10}$$

where ξ is the signed distance from a point $\mathbf{x}$ to an interface Γ. The near tip enrichment functions ψ_α are defined in terms of local coordinates (r, θ) and given as

$$\psi_\alpha(r,\theta) = \left\{ \sqrt{r}\sin\tfrac{\theta}{2},\quad \sqrt{r}\cos\tfrac{\theta}{2},\quad \sqrt{r}\sin\theta\sin\tfrac{\theta}{2},\quad \sqrt{r}\sin\theta\cos\tfrac{\theta}{2} \right\} \tag{4.11}$$

Approximation (4.9) is not an interpolation as nodal parameter $\mathbf{u_i}$ is not the real displacement value at node i. To overcome this shortcoming a shifting procedure is implemented. That is the Heaviside function and near-tip functions are shifted around the node of interest [46].

4.3 Numerical Integration

Numerical integration of the weak form of the governing equation presents a major challenge in XFEM. This is due to the presence of the Heaviside enrichment function which is discontinuous across the crack. In the following section we try to study the effect of crack location on the error in integral value. We consider a single one-dimensional element with crack arbitrary located between the two end nodes (figure 4.2a). The integrands present in the stiffness matrices are bilinear, quadratic and cubic polynomials or the rational polynomials for 4-node quadrilateral element. Therefor, we consider three different cases with following types of integrals for one-dimensional study.

1. Function in the integrand is linear that is $I = \int_{-1}^{1} xH(x)dx$
2. Function in the integrand is quadratic that is $I = \int_{-1}^{1} x^2H(x)dx$
3. Function in the integrand is cubic that is $I = \int_{-1}^{1} x^3H(x)dx$

Where $H(x)$ is the discontinuous Heaviside function which, for our one-dimensional case, is defined as

$$H(x) = \begin{cases} 1 & \forall x > 0 \\ -1 & \forall x < 0 \end{cases} \tag{4.12}$$

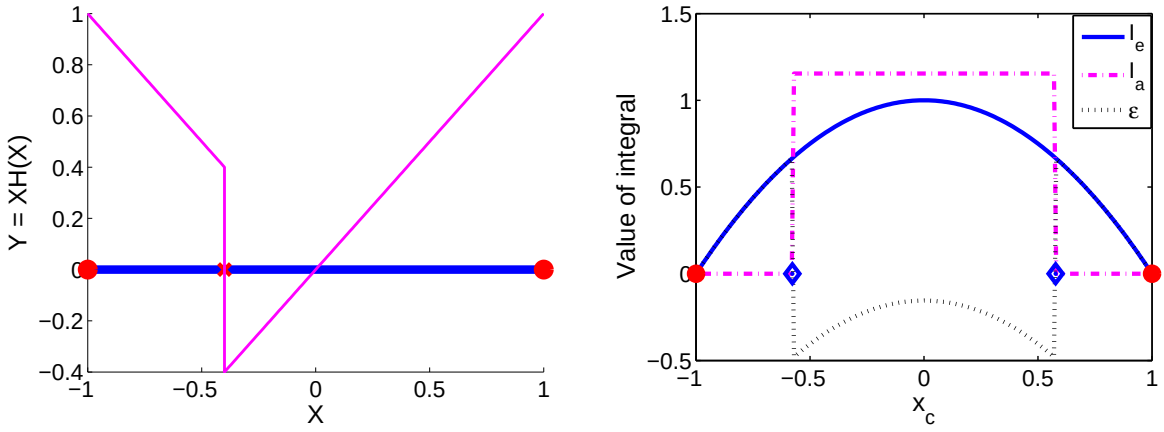

(a) (b)

Figure 4.2: (a) Variation of $xH(x)$ along the element for a crack arbitrary located at x_c (marked with "×"). (b) Error in integral vs. crack position for integral $I = \int_{-1}^{1} xH(x)dx$. Nodes are marked with circles and Gauss points are marked with "◇" markers.

The exact value of the integral (I_e) is obtained by integrating the function analytically as follows.

$$I_e = \int_{-1}^{1} f(x)H(x)dx = -\int_{-1}^{x_c} f(x)dx + \int_{x_c}^{1} f(x)dx \tag{4.13}$$

For numerical evaluation of integrals we use the Gauss quadrature rule. The Gauss quadrature rules with n points are exact for integrating polynomials of degree up to $2n-1$. Therefore we use 2-point Gaussian quadrature rule to evaluate integral numerically. The 2-point Gauss rule can integrate polynomials of degree up to 3 exactly. According to Gauss quadrature rules numerically evaluated integral is given as

$$I_a = \int_{-1}^{1} f(x)H(x)dx = \sum_{i=1}^{2} f(x_i)H(x_i)w_i \tag{4.14}$$

where x_i and w_i are the integration points and associated weights, respectively. Error in integration is defined as

$$\epsilon = I_e - I_a \tag{4.15}$$

Figure 4.2a shows the variation of discontinuous function $xH(x)$ (case "1") along the

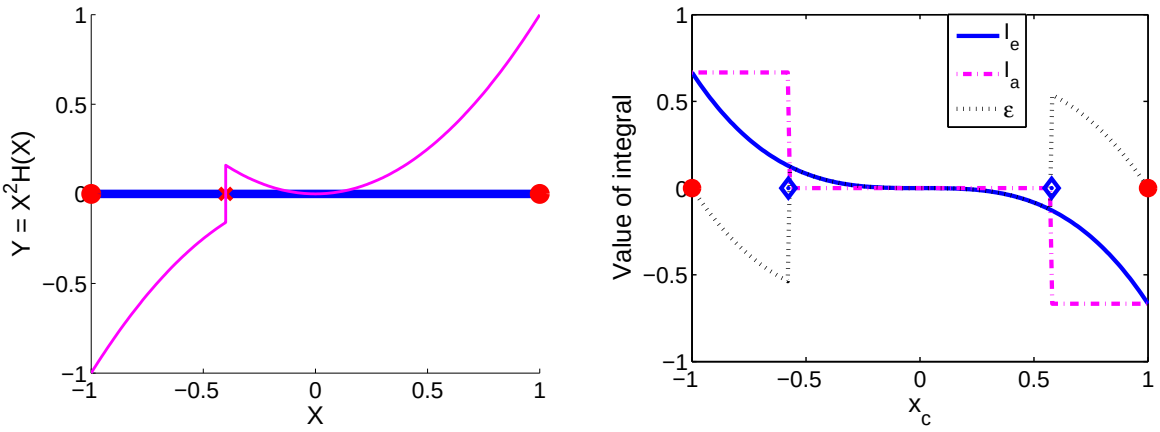

(a) (b)

Figure 4.3: (a) Variation of $x^2H(x)$ along the element for a crack arbitrary located at x_c (marked with "×"). (b) Error in integral vs. crack position for integral $I = \int_{-1}^{1} x^2H(x)dx$. Nodes are marked with circles and Gauss points are marked with "⋄" markers.

element for a crack arbitrary located at x_c. Figure 4.2b shows the value of integrals and error in integral value versus crack position for case "1". An error of -0.1547 is observed when the crack is located at origin. Error is maximum at Gauss points with a value of 0.6636. As the crack is moved from Gauss points towards nodes the error keeps on decreasing and finally becomes zero at nodes. Figure 4.3a shows the variation of discontinuous function $xH(x)$ (case "2") along the element for a crack arbitrary located at x_c. The value of integrals for this case versus crack location is shown in figure 4.3b. The error in integral value is zero when the crack is located at the center. The error continues to increase as the crack is moved towards either of the Gauss points and reaches to 0.123. The error jumps to -0.536 just after the Gauss points then continues to decrease as the crack is moved towards nodes and become zero at nodes. Figure 4.4a shows the variation of discontinuous function $x^3H(x)$ (case "3") along the element for a crack arbitrary located at x_c. Figure 4.3b shows the value of integral as function of crack position for this case. The error at origin is 0.115 and continues to decrease towards either of the Gauss points and reaches to 0.062 as the crack approaches the Gauss points.

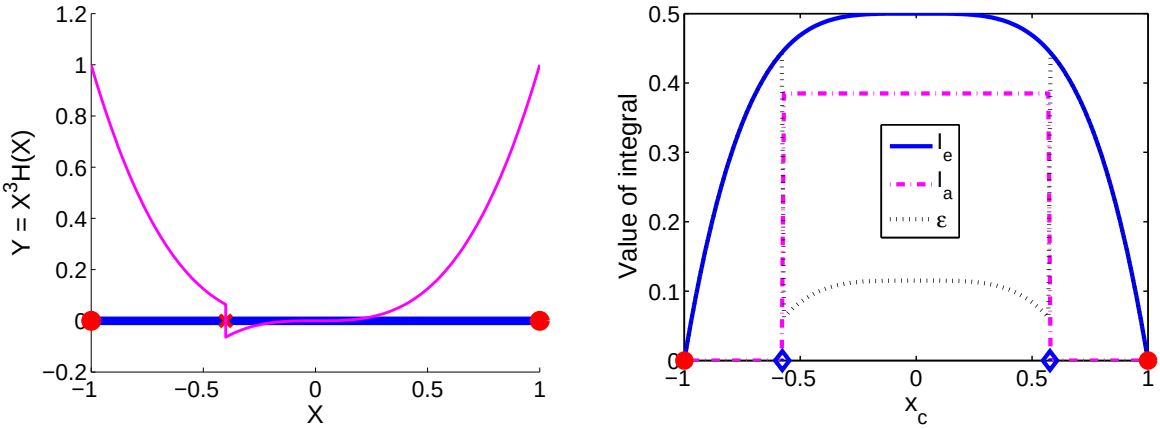

(a) (b)

Figure 4.4: (a) Variation of $x^3H(x)$ along the element for a crack arbitrary located at x_c (marked with "$\times$"). (b) Error in integral vs. crack position for integral $I = \int_{-1}^{1} x^3 H(x) dx$. Nodes are marked with circles and Gauss points are marked with "$\diamond$" markers.

The error jumps to 0.443 just after the Gauss points and continues to decrease towards nodes and becomes zero at nodes.

From the above discussion we can conclude that the error is less when the crack is located either near to the origin or near to either of the nodes. In all other cases error is very high. As we have seen that even for one dimensional case the Gaussian quadrature gives inaccurate results (except only for few special cases) for integrals involving discontinuous functions, we divide the element into sub-elements. And hence the integrands become continuous on each sub-elements. For elements intersected by crack, we modify the element quadrature routines to accurately assemble the contribution to the weak form on both sides of the discontinuity. The discrete weak form is usually constructed with a loop over all elements, as the domain is approximated by

$$\Omega = \sum_{e} \Omega_e$$

where Ω_e is the element subdomain. For elements cut by a crack, we define the element sub-domain to be a sum of a set of sub-polygons (Ω_s) whose boundaries align with the

crack geometry

$$\Omega_e = \sum_s \Omega_s$$

We divide the elements into triangles. The subpolygons are only necessary for integration purposes as no additional degrees of freedom are associated with their construction. In the integration of the weak form, an additional loop over sub-polygons is incorporated for the elements that are divided into sub-polygons.

Although in case of elements with tip enrichments there is no discontinuous field, we still subdivide the elements into sub-elements. This is done in order to capture the effect of high stress gradients in the vicinity of the crack. We generally refer to intersected elements as well as blending elements as enriched elements. We use the following two different numerical integration scheme based on the element type.

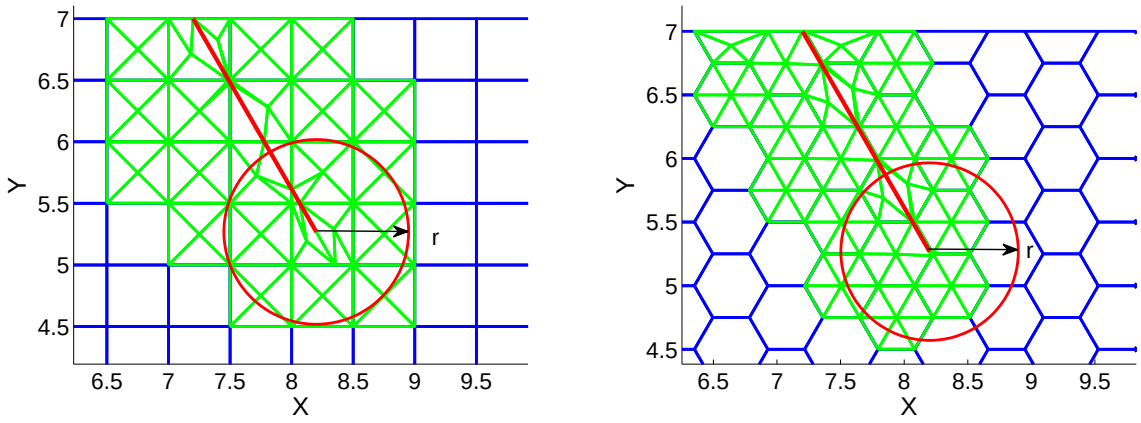

Figure 4.5: Triangulation of enriched elements in (a) quadrilateral and (b) hexagonal structured mesh.

1. Integration on unenriched elements is performed by two-level mapping scheme with optimal integration points for integration as described in chapter 3. An arbitrary polygon is first mapped to a reference polygon using isoparametric mapping. The reference polygon is then mapped to unit circle. The integration is done over this unit disc. We use 4, 5 and 6 optimal integration points for 4-node quadrilateral

element, 5-node pentagonal element and 6-node hexagonal element, respectively. The two-level mapping for hexagonal element is shown in figure 2.4.

2. The integration scheme for enriched elements are similar to the scheme given in Ref. [44] except that we define the Wachspress shape function over this arbitrary physical element for enriched elements as opposed to on reference polygons in Ref. [44]. Hence the need for mapping the integration points from reference polygon to physical polygon is eliminated as done in Ref. [44]. The actual physical polygonal element is then triangulated. Delaunay triangulation algorithm as implemented in software package TRIPACK [47] is used to triangulate the enriched elements. In each subtriangle a 25-point Gauss quadrature rule is used [42]. Triangulation for enriched elements in quadrilateral and hexagonal mesh is shown in figure 4.5a and figure 4.5b, respectively.

4.4 Numerical Results and Discussions

In this thesis the present method has been applied to edge crack in a plate under uniaxial loading (mode 1) and oblique crack under uniaxial loading (mixed mode) problem. The finite element model with boundary conditions is shown in figure 4.6. Convergence of stress intensity factor with number of nodes has been established. For these problems a quadrilateral and a polygonal mesh have been used and two such meshes are shown in figure (4.7). 2D bars of dimensions L=16, W=7 and a=3.5 for mode 1 problem and L=16, W=7, a=2 and $\beta = 60^o$ for mixed mode problem have been considered. Other material properties are: $E = 2$ GPa, $\nu = 0.3$ and far field stress $\sigma = 1$ MPa. The reference solution for edge crack in a plate under uniaxial loading is given by [48]

$$K = F(\frac{a}{W})\sigma\sqrt{\pi a} \tag{4.16a}$$

$$F\left(\frac{a}{W}\right) = 1.12 - 0.231\left(\frac{a}{W}\right) + 10.55\Big(\frac{a}{W}\Big)^2 - 21.72\Big(\frac{a}{W}\Big)^3 + 30.39\Big(\frac{a}{W}\Big)^4 \tag{4.16b}$$

where F is the geometry correction factor.

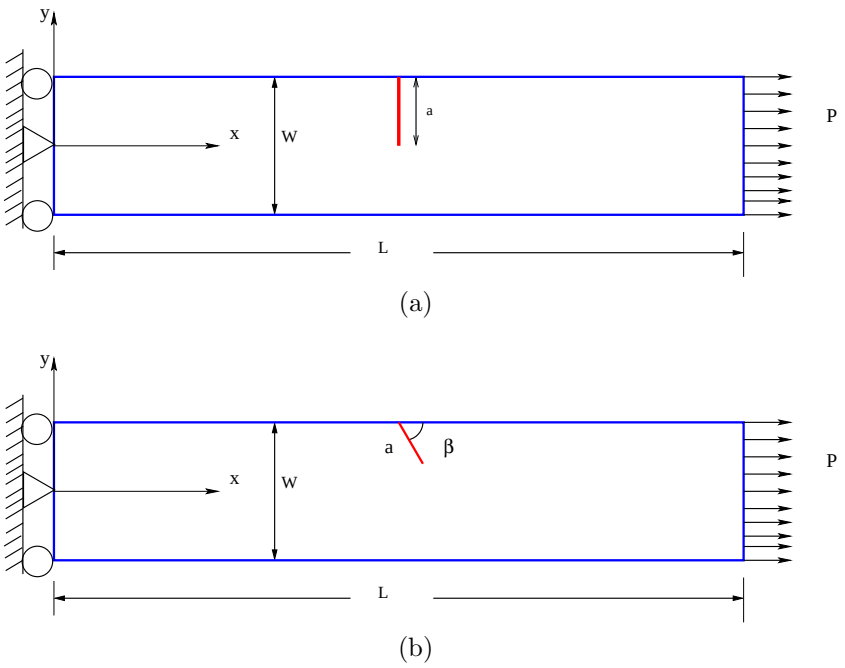

Figure 4.6: Finite element model with boundary conditions. (a) Edge crack. (b) Oblique crack.

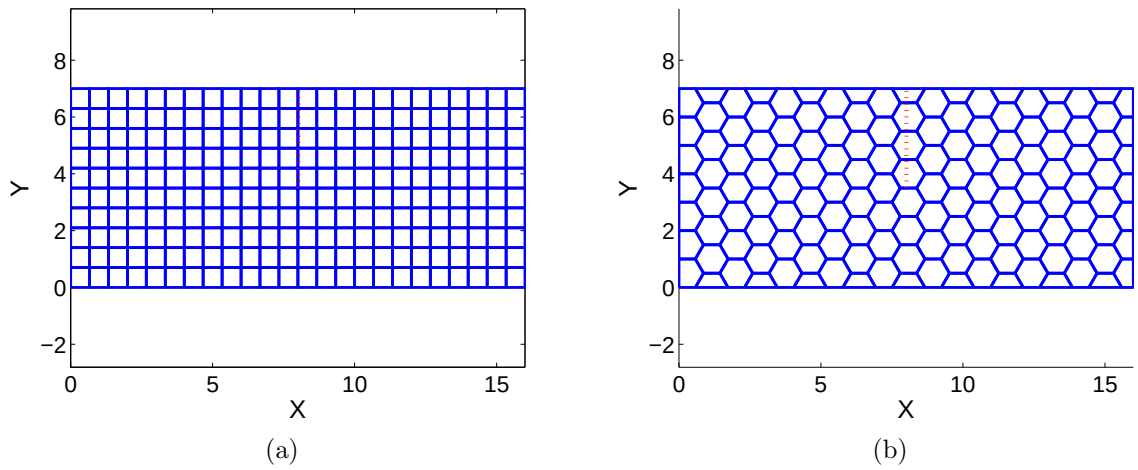

Figure 4.7: (a) Quadrilateral and (b) hexagonal structured mesh.

The geometry factors for stress intensity factors for oblique crack under uniaxial loading are computed from the curves given in Ref. [49].

$$K_I = F_I \sigma \sqrt{\pi a}; \quad K_{II} = F_{II} \sigma \sqrt{\pi a} \tag{4.17}$$

for $\beta = 60^o$

$$F_I = 1.25; \quad F_{II} = 0.3875$$

The domain form of the interaction integral is used to extract the stress intensity factors (SIFs) [50, 48] with a domain radius $r = Rh$ (h is the size of the crack-tip element and is defined as square root of the crack-tip element area). Two different values of J domain factor R, namely $R = 1.5$ and $R = 2.0$ are considered. Details on the extraction of SIFs in the X-FEM can be found in Ref. [4].

We use three different methods to compare the convergence of stress intensity factors. All the three methods use triangulation scheme for integration over enriched elements. The methods differ only in terms of use of integration scheme for unenriched elements. In Method 1 we use standard isoparametric mapping with 2×2 Guass integration in structured quadrilateral finite element mesh. In Method 2 we use optimal integration scheme with SC mapping in structured quadrilateral finite element mesh. In method 3 we use optimal integration scheme with SC mapping for structured hexagonal finite element mesh.

Figure 4.8a shows the convergence of three different methods for $R = 1.5$ for pure mode 1 case. Method 3, that is the optimal integration scheme applied over hexagonal mesh displays faster convergence when compared to two other methods. However in case of factor $R = 2.0$ (fig. 4.8b) all the three methods shows more of less similar kind if trends.

Distribution of 3 different types of stress, namely σ_{xx}, σ_{yy} and σ_{xy}, for pure mode 1 case is considered next. Figure 4.9 shows the element-wise (non-smoothed) distribution of stresses in the vicinity of crack for converged results for method 2. We see the sudden change in stress field across the boundaries of elements. Therefore the stress smoothing

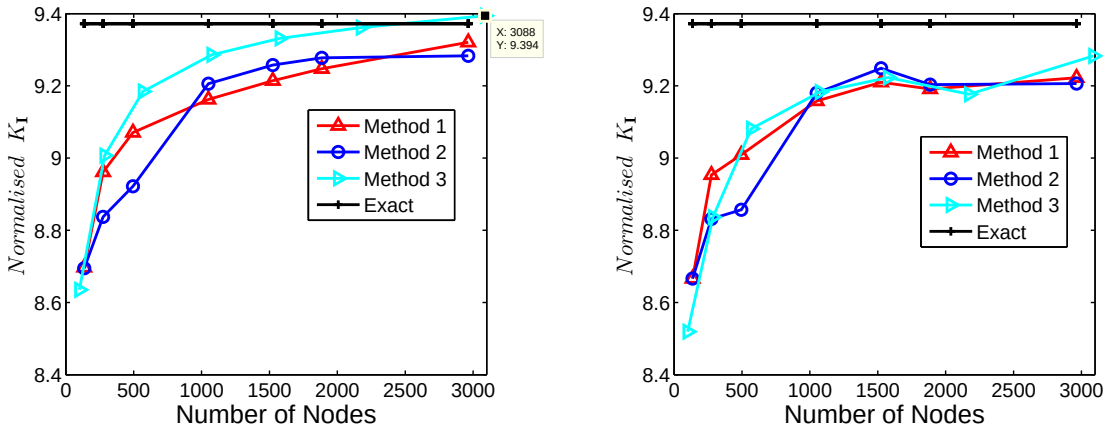

(a) (b)

Figure 4.8: Convergence in mode 1 SIF for edge crack under uniaxial loading for (a) R = 1.5. (b) R = 2.0.

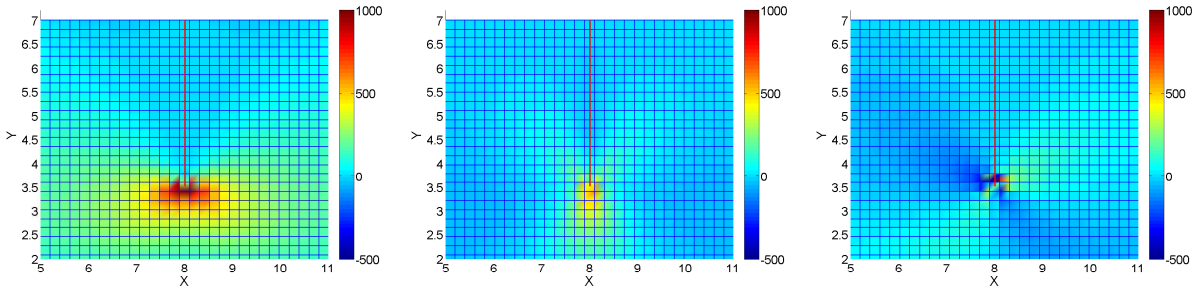

(a) (b) (c)

Figure 4.9: Element wise stress distribution (non-smoothed) for straight edge-crack under uniaxial loading for structured mesh using 4-node quadrilateral elements. (a) σ_{xx}. (b) σ_{yy}. (c) σ_{xy}.

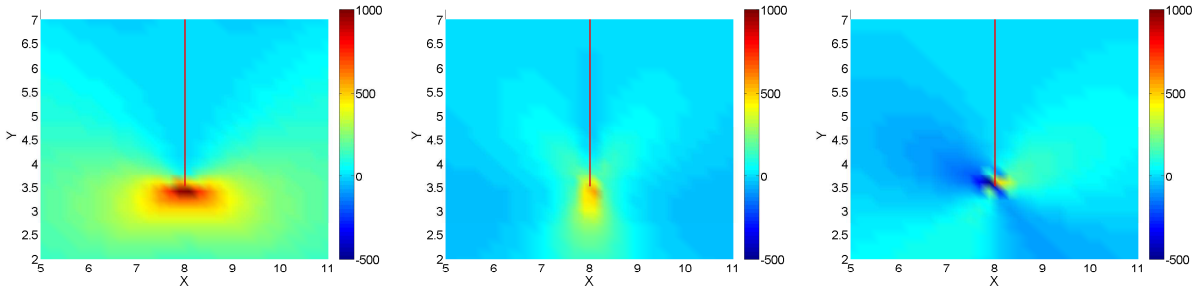

(a) (b) (c)

Figure 4.10: Smoothed (nodal averaging) stress distribution for straight edge-crack under uniaxial loading for structured mesh using 4-node quadrilateral elements. (a) σ_{xx}. (b) σ_{yy}. (c) σ_{xy}.

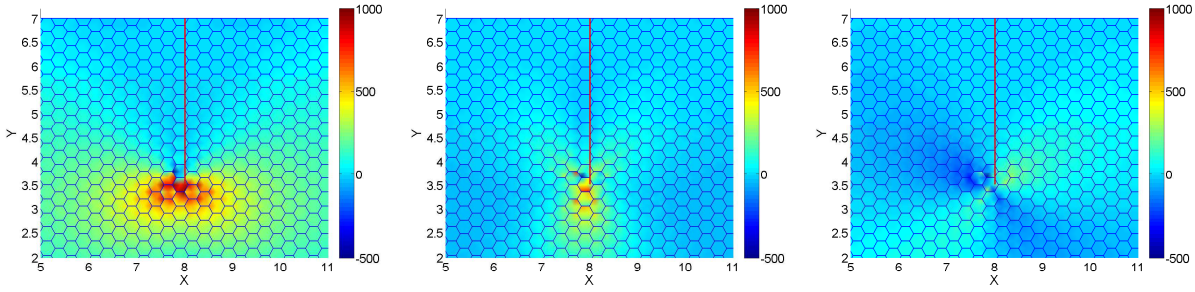

(a) (b) (c)

Figure 4.11: Element wise stress distribution (non-smoothed) for straight edge-crack under uniaxial loading for structured mesh using 6-node hexagonal elements. (a) σ_{xx}. (b) σ_{yy}. (c) σ_{xy}.

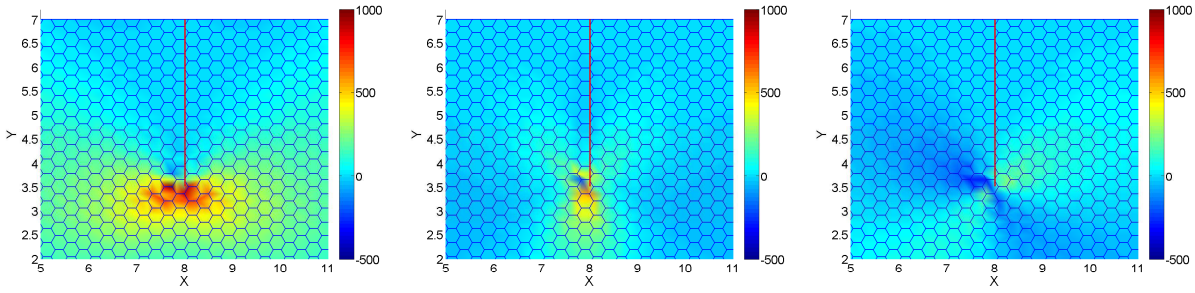

(a) (b) (c)

Figure 4.12: Smoothed (nodal averaging) stress distribution for straight edge-crack under uniaxial loading for structured mesh using 6-node hexagonal elements. (a) σ_{xx}. (b) σ_{yy}. (c) σ_{xy}.

is done using nodal stress averaging method. Figure 4.10 shows the smoothed stress field near the crack for method 2. Figures 4.11 and 4.12 show the non-smoothed and smoothed stress fields using method 3, respectively.

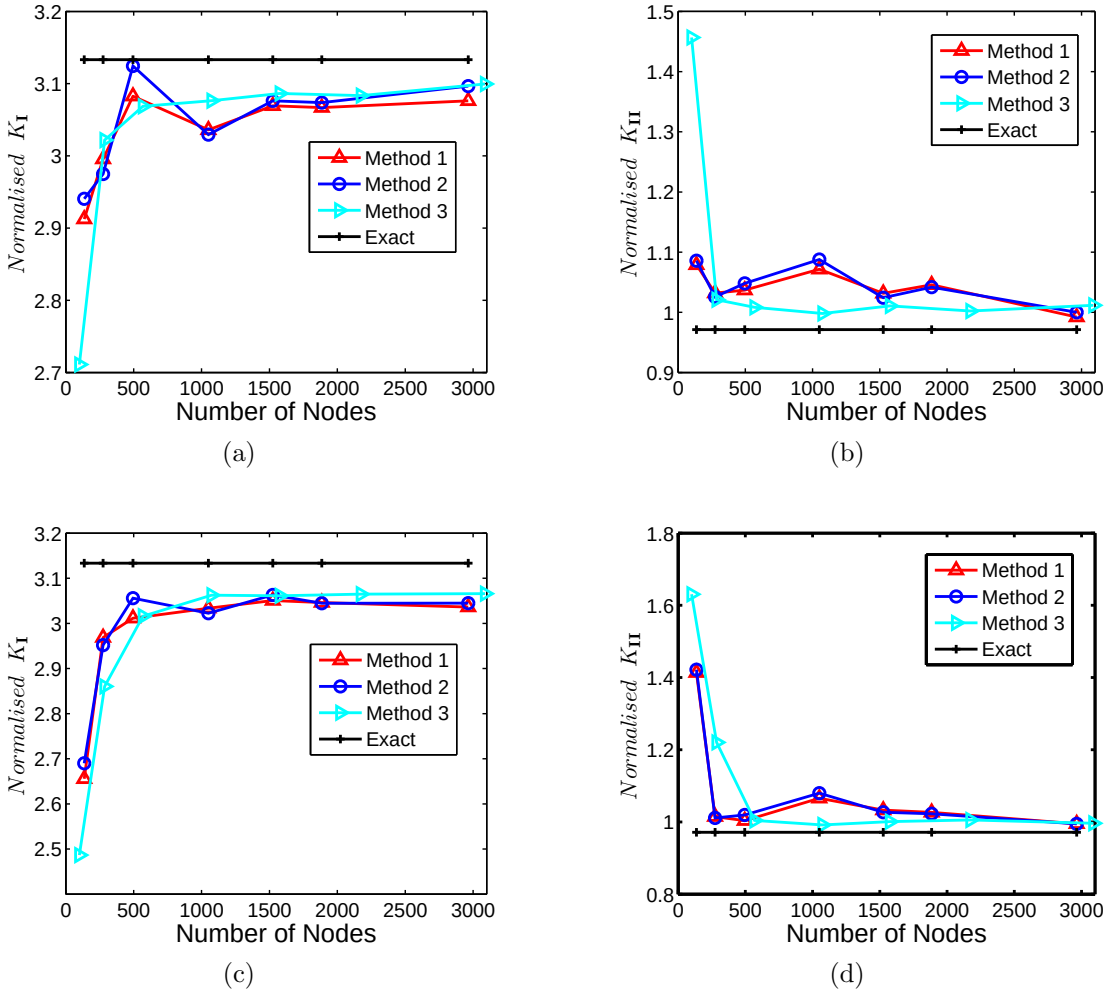

Figure 4.13: Convergence in mixed mode SIFs for oblique crack under uniaxial loading. (a) K_I for R = 1.5. (b) K_{II} for R = 1.5. (c) K_I for R = 2.0. (d) K_{II} for R = 2.0.

Figure 4.13 shows the convergence of mode 1 and mode 2 stress intensity factors for the mixed mode problem. Figures 4.13a and 4.13b shows the convergence of mode 1 and mode 2 stress intensity factors with number of nodes, respectively. Here too the Method 3 shows better convergence rate compared to two other methods. Almost similar kind of results observed for factor $R = 2.0$. However, in latter case the oscillations in

convergence curves are small compared to the former. This might be due to the fact that stress gradients are very high near crack tip. Hence as the J domain radius is increased J integral becomes more and more smooth.

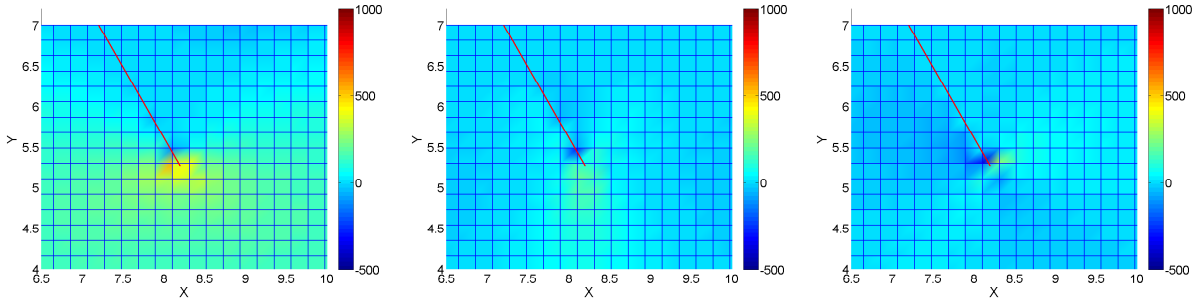

(a) (b) (c)

Figure 4.14: Element wise stress distribution (non-smoothed) for oblique edge-crack under uniaxial loading for structured mesh using 4-node quadrilateral elements. (a) σ_{xx}. (b) σ_{yy}. (c) σ_{xy}.

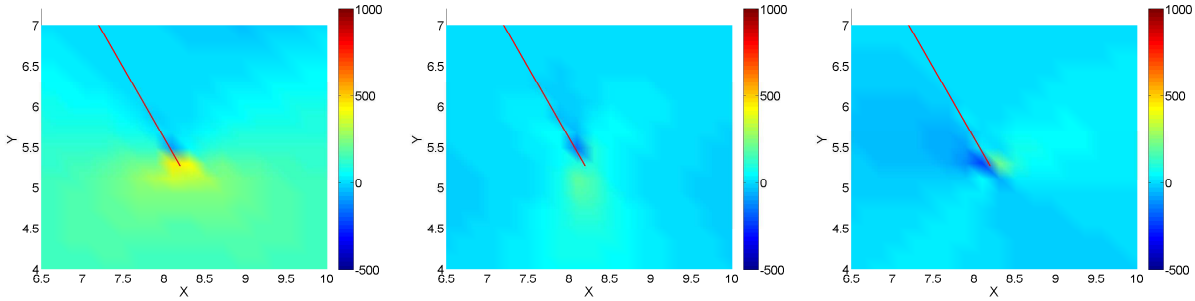

(a) (b) (c)

Figure 4.15: Smoothed (nodal averaging) stress distribution for oblique edge-crack under uniaxial loading for structured mesh using 4-node quadrilateral elements. (a) σ_{xx}. (b) σ_{yy}. (c) σ_{xy}.

Figure 4.14 shows the element-wise (non-smoothed) distribution of stresses near to the crack for converged results using method 2. Here too, we observe the sudden change in stress field across the boundaries of elements. Figure 4.15 shows the smoothed stress field in the vicinity of the crack using method 2. Figures 4.16 and 4.17 show the non-smoothed and smoothed stress fields using method 3, respectively.

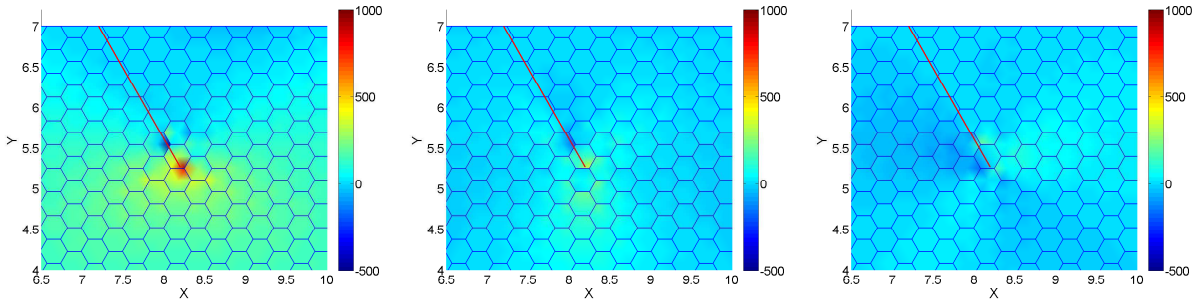

(a) (b) (c)

Figure 4.16: Element wise stress distribution (non-smoothed) for oblique edge-crack under uniaxial loading for structured mesh using 6-node hexagonal elements. (a) σ_{xx}. (b) σ_{yy}. (c) σ_{xy}.

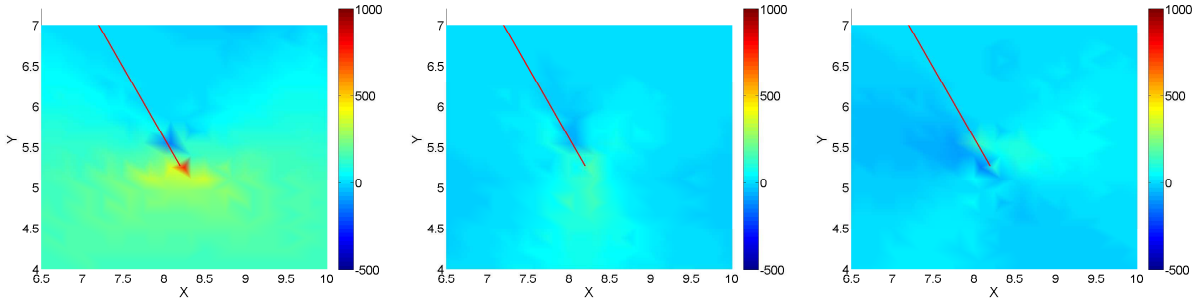

(a) (b) (c)

Figure 4.17: Smoothed (nodal averaging) stress distribution for oblique edge-crack under uniaxial loading for structured mesh using 6-node hexagonal elements. (a) σ_{xx}. (b) σ_{yy}. (c) σ_{xy}.

Chapter 5

Conclusions and Future Work

5.1 Summary of the Completed Work

Polygonal finite elements provide a versatile way to discretize complex geometries which otherwise have been very difficult without compromising the mesh quality and accuracy of results. The method presented in this paper works equally well for structured and unstructured mesh with 4-node quadrilateral, 5-node pentagonal and 6-node hexagonal elements. Also this is first time that successful attempt has been reported to ensure the degeneracy of general polygon to quadrilateral elements with optimal integration points. We show that highly accurate results are obtained without need for large number of integration points. Namely for a typical problem, the strain energy is shown to always converge to the analytical solution at the optimal rate, while previously proposed methods may not converge. The standard problems of uniaxial and shear loadings have been solved for various kinds of polygonal meshes using the optimal integration scheme with very good convergence. Still the method proposed by us has one limitation. We have optimized the integration points only for quadrilateral, pentagonal and hexagonal elements. Higher-order approximations and polygons with more than 6 nodes schemes should be investigated. The proposed method will find useful application in solving elasticity problem with complex geometries, polycrystalline materials, biological tissues and many others. Extension to 3D is not straightforward because of the absence of the 3D

version of the SC mapping. By converting the volume integrals to boundary integrals [8] using strain smoothing and then using the proposed scheme on each face of the polyhedral element is a possibility. This has direct application to integrate discontinuous terms appearing in the weak form of XFEM problems for cracks or material interfaces for example.

We have also applied the new scheme for determination of pure mode 1 and mixed mode stress intensity factors using polygonal finite elements. Convergence rates are also comparable to other standard finite element methods. Error in calculated stress intensity factors is less then 3 %. We applied the scheme only for edge cracks as they are more severe compared to other kind of cracks. However the scheme can be extended to any kind of cracks. The thesis also establishes the applicability of optimal integration scheme introduced in this thesis for polygonal finite elements to fracture mechanics problems based on XFEM approach. We have only considered the structured quadrilateral and structured hexagonal mesh. But it should be possible to extend to method to unstructured meshes as well. In fact the real application of the method lies in cases where it becomes very difficult to mesh the geometries due to their complex shapes.

5.2 Application and Future Work

The proposed method will find useful application in solving elasticity problem with complex geometries, polycrystalline materials, biological tissues and many others. Most of the engineering materials have polycrystalline microstructure. Hence the method could be used to model the physics of microstructures into the finite element model. The proposed method could also be extended to find the natural frequencies of structures with strong and weak discontinuities in XFEM framework. The another promising application is to model the intergranular and intragranular crack growth in polycrystalline materials.

Bibliography

[1] Chan SK, Tuba IS, Wilson WK. On finite element method in linear fracture mechanics. *Engineering Fracture Mechanics* 1970; **2**:1–17.

[2] Li FZ, Shih CF, Needleman A. A comparison of methods for calculating energy release rates. *Engineering Fracture Mechanics* 1985; **21**(2):405–421.

[3] Belytschko T, Black T. Elastic crack growth in finite elements with minimal remeshing. *International Journal for Numerical Methods in Engineering* 1999; **45**:601–620.

[4] Moës N, Dolbow J, Belytschko T. A finite element method for crack growth without remeshing. *International Journal for Numerical Methods in Engineering* 1999; **46**:131–150.

[5] Dolbow JE. An extended finite element method with discontinuous enrichment for applied mechanics. PhD dissertation, Theoretical and Applied Mechanics, Northwestern University, USA.

[6] Natarajan S, Mahapatra DR, Bordas S. Integrating strong and weak discontinuities without integration subcells and example applications in an XFEM/GFEM framework. *International Journal for Numerical Methods in Engineering* 2010; Article in Press. DOI: 10.1002/nme. 2798.

[7] Liu GR, Dai KY, Nguyen TT. A smoothed finite element for mechanics problems. *Computational Mechanics* 2007; **39**(6): 859–877.

[8] Chen JS, Wu CT, Yoon S, You Y. A stabilized conforming nodal integration for Galerkin mesh-free methods. *International Journal for Numerical Methods in Engineering* 2001; **50**:435–466.

[9] Natarajan S, Bordas S, Mahapatra DR, Pont SD, Rabczuk T, Noel D, Guo Z. On the smoothed extended finite element method. *International Journal for Numerical Methods in Engineering* 2009; **00**:1–6.

[10] Bordas S, Rabczuk T, Hung N, Nguyen VP, Natarajan S, Bog T, Quan DM, Hiep NV. Strain smoothing in FEM and XFEM. *Computers & Structures* 2008; Article in Press. DOI:10.1016/j.compstruc.2008.07.006.

[11] Wachspress EL. A rational basis for function approximation. *Lecture notes in Mathematics*; 1971.

[12] Malsch EA, Dasgupta G. Shape functions for polygonal domains with interior nodes. *International Journal for Numerical Methods in Engineering* 2004; **61**:1153-1172.

[13] Sukumar N, Tabarraei A. Conforming polygonal finite elements. *International Journal for Numerical Methods in Engineering* 2004; **61**:2045–2066.

[14] Meyer M, Lee H, Barr AH. Generalized barycentric coordinates for irregular n-gons. *Journal of Graphics Tools* 2002; **7**(1):13–22.

[15] Floater MS. Mean value coordinates. *Computer Aided Geometric Design* 2003; **20**:19-27.

[16] Sukumar N, Malsch EA. Recent advances in the construction of polygonal finite element interpolants. *Archives of Computational Methods in Engineering* 2006; **13**(1):129–163.

[17] Sukumar N. Construction of polygonal interpolants: A maximum entropy approach. *International Journal for Numerical Methods in Engineering* 2004; **61**(12):2159–2181.

[18] Nguyen VP, Rabczuk T, Bordas S, Duflot M. Meshless methods: A review and computer implementation aspects. *Mathematics and Computers in Simulation* 2008; **79**(3):763–813.

[19] Wandzura S, Xiao H. Symmetric quadrature rules on a triangle. *Computers and Mathematics with Applications* 2003; **45**:1829-1840.

[20] Natarajan S, Bordas SP, Mahapatra DR. Numerical integration over arbitrary polygonal domains based on schwarz-christoffel conformal mapping. *International Journal for Numerical Methods in Engineering* 2009; **80**:103–134.

[21] Suvranu D, Bathe KJ. The method of finite spheres with improved numerical integration. *Computers and structures* 2001; **79**(1).

[22] Dasgupta Gautam. Interpolants within convex polygons: Wachspress' shape functions. *ASCE - Journal of aerospace engineering* 2003; **16**:1–8.

[23] Cueto E, Sukumar N, Calvo B, Martínez MA, Cegoñino J, Doblaré M. Overview and recent advances in natural neighbour galerkin methods. *Archives of Computational Methods in Engineering* 2003; **10**(4):307–384.

[24] Sukumar N, Moran B, Belytschko T. The natural element method in solid mechanics. *International Journal for Numerical Methods in Engineering* 1998; **43**(5):839–887.

[25] Arroyo M, Ortiz M. Local Maximum-entropy Approximation Schemes. *Lecture Notes in Computational Science and Engineering,* vol. 57 Springer: Berlin, 2006; 1-16.

[26] Arroyo M, Ortiz M. Local maximum-entropy approximation schemes: a seamless bridge between finite elements and meshfree methods. *International Journal for Numerical Methods in Engineering* 2006; **65**(13):2167-2202.

[27] Sukumar N. Maximum entropy approximation. *Bayesian Inference and Maximum Entropy Methods in Science and Engineering* 2005; **803**:337344.

[28] Sukumar N, Wright R. Overview and construction of meshfree basis functions: from moving least squares to entropy approximants. *International Journal for Numerical Methods in Engineering* 2007; **70**:181-205.

[29] Warren J, Schaefer S, Hirani A, Desbrun M. Barycentric coordinates for convex sets. *Advances in Computational Mechanics* 2007; **27**(3):319–338.

[30] Zwiluncer D. *CRC Standard Mathematical Tables and Formulae,* (31st edn) Chapman & Hall/CRC:2003.

[31] Warren J. On the uniqueness of barycentric coordinates. *Contemporary Mathematics: Proceedings of AGGM02* 2003; :93–99.

[32] Nguyen-Xuan H, Bordas S, Nguyen-Dang H. A smoothed finite element method for shells. *Computer Methods in Applied Mechanics and Engineering* 2008; **198**:165–177.

[33] Chen JS, Wang HP. Some recent improvements in meshfree methods for incompressible finite elasticity boundary value problems with contact. *Computational Mechanics* 2000; **25**:137–156.

[34] Bordas S, Natrajan S. On the approximation in the smoothed finite element method. *International Journal for Numerical Methods in Engineering* 2010; **81**:660–670.

[35] Mousavi SE, Xiao H, Sukumar N. Generalized Gaussian quadrature rules on arbitrary polygons. *International Journal for Numerical Methods in Engineering* 2010; **82**:99–113.

[36] Trefethen LN, Numerical computation of the schwarz-christoffel transformation. *SIAM Journal of Scientific and Statistical Computing* 1980; **1**:82–102.

[37] Driscoll TA, Trefethen LN. Algorithm 756: a matlab tool box for Schwarz Christoffel mapping. *ACM Transactions on Mathematical Software* 1996; **22**(2):168-186.

[38] Driscoll TA, Trefethen LN. Schwarz-Christoffel mapping. *Cambridge Monographs on Applied and Computational Mathematics* 2002; **8**(1).

[39] Timoshenko SP, Goodier JN. *Theory of Elasticity,* McGraw-Hill: New York: 1970.

[40] Augarde CE, Deeks AJ. The use of Timoshenkos exact solution for a cantilever beam in adaptive analysis. *Finite Elements in Analysis and Design* 2008; **44**:595–601.

[41] Golub GH, Loan CFV. *Matrix Computations,* (3rd edn) The John Hopkins University Press:Baltimore and London:1996; 58–59.

[42] Dunavant DA. High degree efficient symmetrical Guassian quadrature rules for the triangle. *International Journal for Numerical Methods in Engineering* 1985; **21**:1129–1148.

[43] Babuska I, Melenk JM. The partition of unity method. *International Journal for Numerical Methods in Engineering* 1997 **40**:727–758

[44] Tabarraei A, Sukumar N. Extended finite element method on polygonal and quadtree meshes. *Computer Methods in Applied Mechanics and Engineering* 2007; **197**:425–438.

[45] Singh S, Natarajan S, Mahapatra DR, Bordas S. Optimal numerical integration schemes for polygonal finite elements. *International Journal for Numerical Methods in Engineering* 2010; Paper under review.

[46] Mohammadi S. *Extended Finite Element Method,* (1st edn) Blackwell Publishing:2008

[47] Renka RJ, Algorithm 751: TRIPACK, A constrained two-dimensional Delaunay triangulation package, *ACM Transactions on Mathematical Software* 1996; **22**(1):1–8

[48] Gdoutos EE. *Fracture Mechanics,* Kluwer Academics Publishers:1993 Boston.

[49] Murakami Y. *Stress Intensity Factors Handbook,* Pergamon Press:1987 Oxford.

[50] Yau J, Wang S, Corten H. A mixed-mode crack analysis of isotropic solids using conservation laws of elasticity. *Journal of Applied Mechanics* 1980; **47**:335–341.